7-15-2009

Multistability in Bursting Patterns in a Model of a Multifunctional Central Pattern Generator.

Matthew Bryan Brooks

MULTISTABILITY IN BURSTING PATTERNS IN A MODEL OF A MULTIFUNCTIONAL CENTRAL PATTERN GENERATOR

by

MATTHEW BROOKS

Under the Direction of Dr. Andrey Shilnikov

ABSTRACT

A multifunctional central pattern generator (CPG) can produce bursting polyrhythms that determine locomotive activity in an animal: for example, swimming and crawling in a leech. Each rhythm corresponds to a specific attractor of the CPG. We employ a Hodgkin-Huxley type model of a bursting leech heart interneuron, and connect three such neurons by fast inhibitory synapses to form a ring. This network motif exhibits multistable co-existing bursting rhythms. The problem of determining rhythmic outcomes is reduced to an analysis of fixed points of Poincare mappings and their attractor basins, in a phase plane defined by the interneurons' phase differences along bursting orbits. Using computer assisted analysis, we examine stability, bifurcations of attractors, and transformations of their basins in the phase plane. These structures determine the global bursting rhythms emitted by the CPG. By varying the coupling synaptic strength, we examine the dynamics and patterns produced by inhibitory networks.

INDEX WORDS: Bifurcation, Bursting, Central pattern generator, Multistability, Polyrhythmicity, Attractors, Heteroclinic, Saddles, Computational neuroscience

MULTISTABILITY IN BURSTING PATTERNS IN A MODEL OF A MULTIFUNCTIONAL CENTRAL PATTERN GENERATOR

by

MATTHEW BROOKS

A Thesis Submitted in Partial Fulfillment of the Requirements for the Degree of

Master of Science

in the College of Arts and Sciences

Georgia State University

2009

MULTISTABILITY IN BURSTING PATTERNS IN A MODEL OF A MULTIFUNCTIONAL CENTRAL PATTERN GENERATOR

by

MATTHEW BROOKS

Committee Co-Chairs: Andrey Shilnikov
Robert Clewley
Gennady Cymbalyuk

Committee: Igor Belykh
Vladimir Bondarenko
Mukesh Dhamala
Michael Stewart

Electronic Version Approved:

Office of Graduate Studies
College of Arts and Sciences
Georgia State University
August 2009

TABLE OF CONTENTS

LIST OF TABLES

LIST OF FIGURES

1. INTRODUCTION

Neuron Structures and Properties

One of the principal goals of mathematical and computational neuroscience is to provide accurate models that possess or mimic the physical and chemical mechanics of neurons, as well as to construct theories on how those representative models might interact and perform within a set of analytical bounds. Neurons, organized into networks numbering in the thousands in higher order animals, give rise to a level of complexity that only recently has begun to be researched more thoroughly. The evolution of these neuronal networks is thought to come about as a means of transmitting information in an animal's nervous system, relaying messages that produce memory, locomotion, involuntary and voluntary motor reflexes, visual and even hallucinatory phenomena, and other sensory responses (Marder, et al., 1996; Gutkin, et al. 2003). To produce this activity, neuronal networks are organized into smaller interconnected networks whose repetitive electrical rhythms generate these types of motor responses. The basic neural circuits form what are known as *central pattern generators* (CPGs) and formulate the basis of neuronal activity in vertebrate and invertebrate species alike (Marder, et al., 1996). A number of studies have reported on the mechanics and models whereby a significantly limited network of oscillators can yield different qualitative states, especially with neurons associated with locomotive activity; this special feature is referred to as *multifunctionality* (Ashwin, et al., 2008; Canavier, et al. 1999). Our focus for this study is centered on small scale multifunctional neuronal networks and the multistable outcomes that arise as a result of varying external factors such as the strength of electrical currents and relative time periods in which individual bursting activity is initiated.

We briefly introduce the electrophysiological concepts of the neuron in order to provide a cursory foundation for the behaviors exhibited in the systems studied during the course of this work. Consider then the neuron as a single arbiter of electrical activity: a typical neuron contains concentrations of Na^+, K^+, Cl^-, and Ca^{2+} ions, which are separated via a membrane from the extracellular medium which contains

different concentrations of the same ions. The membrane then represents the potential difference between the collections of charges in the two mediums. We refer to this as the *membrane voltage*, and it is the basis for voltage data collected from the models studied here. For the purposes of most of the models described in this work, the voltage is assumed to be uniform across the membrane, although more intricate models may reflect real differences between membrane voltage along the axon and dendritic components of the cell (Izhikevich, 2007).

Changes in ionic concentration, and therefore membrane voltage, precipitate flows of ions across the membrane; this transfer is referred to as the concentration gradient, or *ionic current*. As positively (negatively) charged ions flow out of the cell, they leave behind negatively (positively) charged counterparts which cannot pass through the membrane, lowering the membrane potential. The *equipotential* is reached when the membrane potential is equal to the force exerted by the concentration gradient. Each ionic current, then, is associated with a type of ionic channel. Physiologically, the neuron membrane is comprised of a number of these channels in varying proportions with respect to the type of ion species. Ionic channels are voltage regulated (or *gated*), meaning that they may be open or closed depending on the strength of the membrane potential. We can view then the current I for a particular channel as

$$I = gp(V - E)$$

where g represents the maximal conductance, E is the equipotential, and p is a probability function that reflects the proportion of gates that are open, allowing ions to pass through the membrane. Channels based on this model may be grouped into four types, shown in the table below (Table 1.1).

We geometrically portray the behavior that this electrochemical system effectively produces. Consider the diagram below of a single voltage spike produced by an applied current (Figure 1.1). We observe that before the current is applied, the neuron is in a quiescent state. In a typical neuron, there exists high concentrations of K^+ ions internally and high concentrations of Na^+ and Cl^- ions externally.

Table 1.1. Ionic channels: Behavior and examples (from Terman, et al., 2002; Izhikevich, 2007).

Channel type	Action	Examples
Activation	Opens voltage gated channels. For Na^+ currents, inflow increases membrane potential. For K^+ currents, outflow decreases membrane potential. The closure of activated gate is called deactivation.	Fast transient Na^+ in rat thalamocortical neurons and squid giant axons. Fast transient K^+ in GPe cells in the basal ganglia.
Inactivation	Closes voltage gated channels. For Na^+ currents, membrane potential decreases. For K^+ currents, membrane potential increases. The opening of inactivated gates is called deinactivation.	Delayed rectifier K^+ current in neocortical pyramidal neurons.

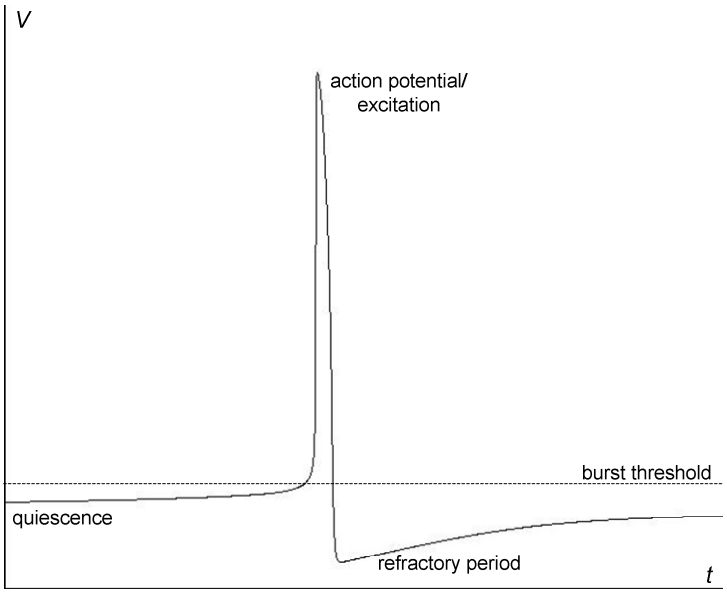

Figure 1.1. Anatomy of a voltage spike produced along a neuron's membrane.

The applied current *depolarizes* the neuron, pushing it towards an excited state. Once the current is sufficient for the voltage to pass the bursting threshold, the neuron responds by firing an *action potential*, or a sharp increase in the membrane voltage. During this period, the ionic channels for Na^+ and K^+ are opened and cause the cations to flow in and out of the cell respectively. The conductance g for Na^+ increases sharply, signifying that the channel is activated. Following this peak the neuron returns to its

resting state, which may be a near instantaneous change in potential or a gradual decline, depending on the rate at which the activation/deactivation takes place. Neurons can also be pushed back into a rest state by the introduction of external *hyperpolarizing* currents, i.e. currents that decrease the overall membrane potential.

In certain models, there exists a *refractory period* that precedes the resting state, a short interval of time where the neuron cannot achieve a spiking state, particularly when an inactivation current is present; absolute refractory states are generally immune to any depolarizing action. Excitability (and therefore the potential for spiking activity) returns only as the inactivation current becomes deinactivated.

The Neuron as a Dynamical System

In order to simulate neuronal behaviors, we want to represent the neuron in the form of a mathematical model that reproduces some of the physical processes that comprise the neuron's structure. We first must consider how "real life" neurons alternate between periods of spiking behavior and quiescence; virtually every neuron studied is based on this characteristic. Information is relayed from one neuron to the next in the form of *action potentials*, or abrupt changes in membrane voltage as a result of shifting changes in ion concentrations in the internal and external cellular media, necessarily perturbing neurons in the vicinity. Thus, any accurate model of the neuron must acknowledge a system where there exists periods of inactivity or very little shift in voltage alternating with periods of intense spiking activity. Voltage then is observed as function over time and is perturbed by changes in other electrophysical properties of the cell, such as inactivation and activation gating voltages associated with different ion concentrations. Additionally, a more comprehensive model must exhibit neuronal properties, such as non-transient spiking, quiescence, and variances in burst frequency (the number of spikes produced in a burst), interspike interval (the duration between two action potential peaks) and duty cycle (the ratio of burst duration to complete burst cycle).

There are a number of ways to represent this basic type of model, depending on the degree to which accurate mechanics are desired versus computational expediency. Simple integrate-and-fire models as well as discrete models have been shown to demonstrate some of the behaviors common to neuronal spiking and bursting activity (Cazelles, et al., 2001; Rulkov, 2002; Rulkov, et al., 2004). As such, these models are very efficient to compute, and they still exhibit many (but not all) of the same phenomena that are present in more comprehensive models. For the purposes of our discussion, we will utilize a continuous dynamical system that closely represents the activities of a physical neuron, albeit with some characteristics that are commonly featured in both continuous and discrete models aimed at characterizing burst activity (Shilnikov, 2004; Rabinovich, et al., 2006).

Quiescence, Spikes, and Bursts

We begin with a discussion of the properties of the typical states of neuronal activity. Consider that the state of a neuron can be viewed as the sum total of the electrical currents passed through it, particularly activation and inactivation currents associated with ion species. Altering the combinations of these currents plays a role in influencing the type of excitation produced by the neuron (Terman, 2004). As these currents are modified, one of several primary transitions can occur with respect to membrane potential:

Table 1.2. Common actions produced by passing current through the neuron membrane.

Activity	Characteristics
Quiescence	No action potentials are generated; the membrane potential changes very little for a specific period of time. A neuron will remain quiescent unless its membrane potential crosses the bursting threshold.
Spiking	Action potentials are generated on a non-transient basis. This is also referred to as *tonic spiking*.
Bursting	Action potentials are generated on a transient basis, and alternate with a resting period.

Sub-threshold Oscillations	Adjustments in current change the membrane potential, but not strongly enough in order to produce action potentials.

Slow-Fast Systems

Variables associated with neuronal activity, such as activation currents, tend to operate on differing time scales. The Na^+ current, for instance, may activate much more rapidly than the corresponding K^+ current. As a result, the neuron can express a large repertoire of dynamical behaviors. To characterize these behaviors, we employ the use of a model known as the *slow-fast system*:

$$\dot{\boldsymbol{x}} = f(\boldsymbol{x}, \boldsymbol{y})$$

$$\dot{\boldsymbol{y}} = \varepsilon g(\boldsymbol{x}, \boldsymbol{y})$$

The vector **x** corresponds to the "fast" subsystem; for the "slow" subsystem, which describes the dynamics of **y**, we introduce a perturbation constant $\varepsilon << 1$. The solutions where $\mathbf{x'=0}$ and $\mathbf{y'=0}$ represent the fast and slow *nullclines* of the system respectively, and the solution $\mathbf{x'=y'=0}$ represents a system *equilibrium*. For our purposes, the slow-fast systems are represented by a set of continuous ODEs, although discrete slow-fast systems exist and are capable of mimicking many of the spiking and bursting behaviors in continuous systems, including bifurcations and chaotic dynamics (Shilnikov, et al., 2002).

To illustrate an example of a slow-fast system, we will briefly describe the example of the Hindmarsh-Rose model, which mimics the principal characteristics of a neuronal system (Shilnikov, et al., 2008):

$$x' = y - ax^3 + bx^2 + \mathrm{I} - \mathrm{z}$$

$$y' = c - dx^2 - y$$

$$z' = \varepsilon(s(x - x_0) - z)$$

In this example, (x,y) and z are the fast and slow systems respectively; parameters a, b, c, and d are static configurations, and x_0 is a bifurcation parameter used to effect changes in the stability of the system. Of particular note are the cubic shape of the fast nullcline and the planar structure of the slow nullcline (Figure 1.2). As a trajectory is computed over time, it tends towards the right in regions where $z'>0$ and tends towards the left as $z'<0$. Additionally, the state of the neuron is in part reflected by the portion of the branch a point on the trajectory resides. Below the $z'=0$ plane, the trajectory moves along the lower branch, corresponding to a quiescent state, and above the $z'=0$ plane the trajectory moves along a manifold that wraps around the upper branch. The changes between these states of the system are bifurcations; for this type of two-dimensional system there are number of different possible bifurcation pairs in the transition between bursting regimes and quiescence. A full classification of these bifurcations is provided by Izhikevich (Izhikevich, 1999; Izhikevich, 2004). As we can see, slow-fast dynamics are central to the transition of bursting and spiking behaviors found in neuronal activity.

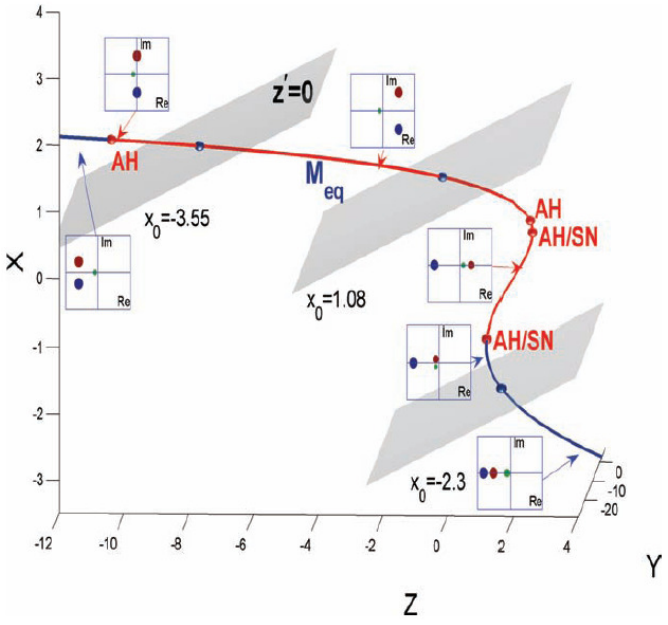

Figure 1.2. Nullclines of the Hindmarsh-Rose system. Insets depict the position of the characteristic exponents in the complex plane. As the planar slow nullcline $z'=0$ is shifted through the branches of the fast nullcline ($x'=y'=0$), the eigenvalues for the plane shift, producing different states of burst activity (taken from Shilnikov, et al., 2008).

Derivation of the Hodgkin-Huxley Model

The original concept of the Hodgkin-Huxley model was derived in 1952 in order to characterize activity in the squid giant axon (Terman, 2004). The model rests on the concept that the neuron is effectively an electrical circuit, which is common to many models of simulated neuronal behavior (Gutkin, et al., 2003). In this setup, we consider that the capacitive current of the membrane itself plus the sum of all of its ionic currents is equal to the total current across the neuron's membrane. We can express this representation in its generalized form with the membrane voltage changing over time:

$$C\frac{dV}{dt} = I_{app} - \sum_{X} I_X(V, w_1, w_2, \dots, w_n)$$

C is the capacitance of the neuron, *X* represents a current of a particular ionic species, w_i represents the set of voltage gated activation variables, and I_{app} is an external current that may be applied to the neuron (often a synaptic current). For each current I_X we have

$$I_X = g_X p_X (V - E_X)$$

Again, as before, g_X is the maximal conductance, and E_X is the equipotential (also referred to as the *reversal potential*) of the species. The term p_X is a probability function, derived from the activation variables w_i, (where $0 \leq w_i \leq 1$) indicating the likelihood that an ionic channel is open. However, the activation variables are non-constant and operate under different time scales. In particular, the dynamics of the activation variables are as follows:

$$\dot{w}_i = \frac{\left[w_{i,\infty}(V) - w\right]}{\tau_{w_i}(V)}$$

$$p_X = w_1^X w_2^X \dots w_n^X$$

Each current I_X may be associated with one or more activation variables, and the functions τ_{wi} represent corresponding time constants.

The basic Hodgkin-Huxley model then is a four dimensional form of the model above:

$$C\frac{dV}{dt} = I_{app} - I_K - I_{Na} - I_L$$

$$= I_{app} - g_K n^4 (V - E_K) - g_{Na} m^3 h (V - E_{Na}) - g_L (V - V_L)$$

$$\frac{dm}{dt} = \frac{[m_\infty(V) - m]}{\tau_m(V)}$$

$$\frac{dn}{dt} = \frac{[n_\infty(V) - n]}{\tau_n(V)}$$

$$\frac{dh}{dt} = \frac{[h_\infty(V) - h]}{\tau_h(V)}$$

The corresponding model above describes the cooperative dynamics of three currents: a persistent K^+ current, a transient Na^+ current, and a leak current (usually from a concentration of Cl^- ions). Variables *m*, *h*, *n* are voltage gating variables corresponding to the activation of the transient current, inactivation of the transient current, and the activation of persistent current, respectively. Finally, the functions $m_\infty(V)$, $n_\infty(V)$, and $h_\infty(V)$ are steady-state activation (inactivation) curves. In simplified versions of the model, the steady state functions are approximated by Boltzmann (sigmoid) functions of the form:

$$X_\infty(V) = \frac{1}{1 + \exp\{(V_{1/2} - V)\theta\}}$$

The shape of this function, normalized to the range [0,1], is influenced by the half-activation voltage $V_{1/2}$ (where $X_\infty(V) = 0.5$) and the slope factor θ (which determines the steepness of the sigmoid function).

Overall, the Hodgkin-Huxley model described above corresponds strictly to the squid axon, which only has three currents. In the case of the leech heart interneuron, the model described above becomes a 14-dimensional system, complete with 5 different time scales (Cymbalyuk, 2005). As we can see, the Hodgkin-Huxley model is easily capable of giving rise to incredibly rich and complicated dynamics. However, attempting to study the dynamics in a 14-dimensional space is computationally challenging at best. In order to observe some of these dynamics (especially in network models containing

multiple neurons), we must apply pharmacological reductions to the system. That is, we must capture the currents that are pertinent to the dynamics being studied, and block the currents that are only marginally influential (Cymbalyuk, et al., 2005; Channell, et al., 2007; Clewley, et al., 2009).

Neuronal Networks

We conclude our review of neuronal models with a discussion of mechanisms for neuronal interactivity. Neurons can operate in two ways: *Inhibitory* neurons yield synaptic current that prevents another neuron's membrane voltage from reaching the burst threshold and causing an action potential, and *excitatory* neurons do exactly the opposite, producing enough current to generate spiking (or bursting) activity. To represent this in the Hodgkin-Huxley model, we introduce a function $s(t)$ to limit the presence of synaptic current for a fixed time interval $[t_{on},t_{off}]$, effectively creating a square wave pulse:

$$s(t) = [H(t - t_{on}) - H(t - t_{off})]$$

$H(t)$ is the Heaviside step function, discretely defined as $H(t) < 0$ when $t < 0$, $H(t) = 1$ when $t > 0$, and $H(t) = ½$ when $t=0$. It follows that the range of $s(t)$, by construction, is [0,1].

This convention becomes particularly useful as we need to create neuronal networks and pass information between them in some meaningful way. As an example, we consider the model of the sub-thalamic nucleus (STN) coupled with a model of the globus pallidus (GPe) cell, corresponding to two groups of neurons that reside in the basil ganglia of the human brain, (Terman, et al., 2002). In a simplified model, the STN generates excitatory responses to structures in the basil ganglia, including GPe cells, which in turn produces action potentials inhibiting STN cells, temporarily hyperpolarizing them until the GPe cells cease firing (Terman, et al., 2002). Figure 1.3 illustrates this behavior over a very limited network of one STN cell and one GPe cell.

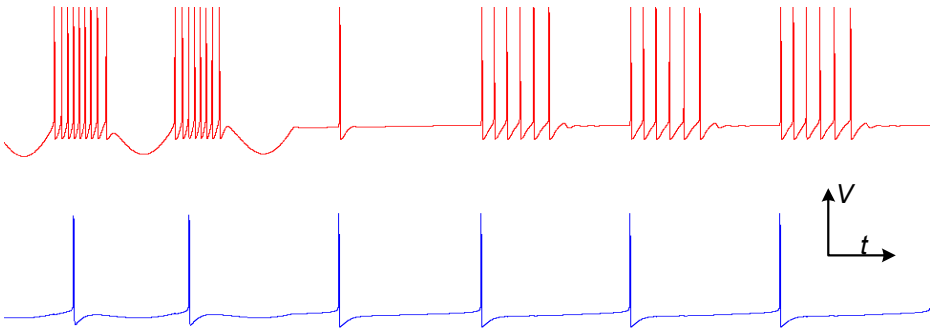

Figure 1.3. Production of action potential firing via depolarization. The excitation response (STN → GPe), shown in blue, is coupled with inhibition of action potential firing via hyperpolarization (GPe → STN), shown in red. The action potential produced by the STN produces excitability in the recipient GPe, while the GPe inhibits the firing of action potentials until the GPe is quiescent, permitting the STN to fire again (model taken from Terman, et al, 2002).

2. BIFURCATIONS AND STABILITY

Equilibria in Systems

We now examine some of the characteristic phenomena that occur in higher dimensional dynamical systems. Consider the generalized slow-fast system described in §1, with $\varepsilon \ll 1$ a perturbation parameter as before. The fast and slow nullclines correspond to $x'=0$ and $y'=0$ respectively, and the solutions to $x'=y'=0$, correspond to equilibria of the complete system. However, we can also determine the stability of the equilibrium point by linearizing the system, provided that f and g are smooth functions. Given a equilibrium point (x^*,y^*) of the system, we may rewrite f and g as follows:

$$\dot{x} = a(x - x^*) + b(y - y^*) + O^2(x, y)$$

$$\dot{y} = c(x - x^*) + d(y - y^*) + O^2(x, y)$$

$O^2(x,y)$ corresponds to higher order terms of the system. The matrix

$$A = \begin{pmatrix} a & b \\ c & d \end{pmatrix} = \begin{pmatrix} f_x & f_y \\ g_x & g_y \end{pmatrix}_{(x,y)=(x^*,y^*)}$$

corresponds to the Jacobian of f, g at (x^*,y^*). We let $\boldsymbol{x} = (x,y)$ and look for solutions to the following equation:

$$A\boldsymbol{x} = \boldsymbol{\lambda x}$$

The solutions λ_1 and λ_2 are produced from the characteristic equation

$$\det|A - \lambda I| = 0$$

and are referred to as the *eigenvalues* of A. The eigenvalues above also generate vectors $\mathbf{u_1}$ and $\mathbf{u_2}$ respectively (known as *eigenvectors*), satisfying the equations above. By looking at the values for λ_1 and λ_2, we can determine the stability of the equilibrium point (x^*,y^*); Table 2.1 provides a list of scenarios and the type of equilibria that are produced.

Table 2.1. Eigenvalues for stability in a two-dimensional system.

λ_1 , λ_2	Equilibrium type
Two distinct real roots with opposite signs. ($\lambda_1 \neq \lambda_2$)	The equilibrium is a saddle, which is classified as unstable since one eigenvalue is positive.
Two distinct real roots with same sign ($\lambda_1 \neq \lambda_2$)	The equilibria is a node, which can be unstable (λ_1 , $\lambda_2 > 0$) or stable (λ_1 , $\lambda_2 < 0$)
Complex conjugates (λ_1, $\lambda_2 = a \pm bi$)	The equilibria is a focus, which can be stable ($a < 0$) or unstable ($a > 0$).

Thus, we have an analytical means for evaluating the stability of an equilibrium point in a higher order system with smooth nullclines. The fact that the neighborhood around the equilibrium behaves equivalently to that of a linear system is a result derived from the Hartman-Grobman theorem (Guckenheimer, et al., 2002).

Bifurcations of Co-dimension 1

A *bifurcation* is a transition in stability in a dynamical system. As systems shift between different states of stability, we can model phenomena that also transition among different types of behaviors. In the context of neurons, bifurcations occur when the neuron approaches a state of excitability, allowing perturbations to shift in a bursting or spiking state and vice versa (Izhikevich, 1999). Both of these transitions are modeled by a various combination of bifurcations. Below, we discuss several classes of bifurcations that are common to higher order dynamical systems, but for simplicity we merely present the two-dimensional representation of the bifurcations we will encounter in this work. Furthermore, all of the bifurcations considered below are *codimension-1*, meaning that a single parameter (referred to as the *bifurcation parameter*) is changed in order to achieve the change in system stability.

Fold bifurcations

Fold (or *saddle node*) bifurcations can be geometrically viewed as a transition where, through changes in the bifurcation parameter, the system gives rise to two equilibria, one stable and one saddle (Figure 2.1). Mathematically, saddle node bifurcations must satisfy three principal conditions: *non-hyperbolicity* ($\lambda_1=0$, $\lambda_2 = a+ib$ with $a\neq0$), *non-degeneracy* (the second order derivatives of f,g are non-zero at the bifurcation point), and *transversality* (the first order partial derivative of f, g with respect to the bifurcation parameter itself is non-zero).

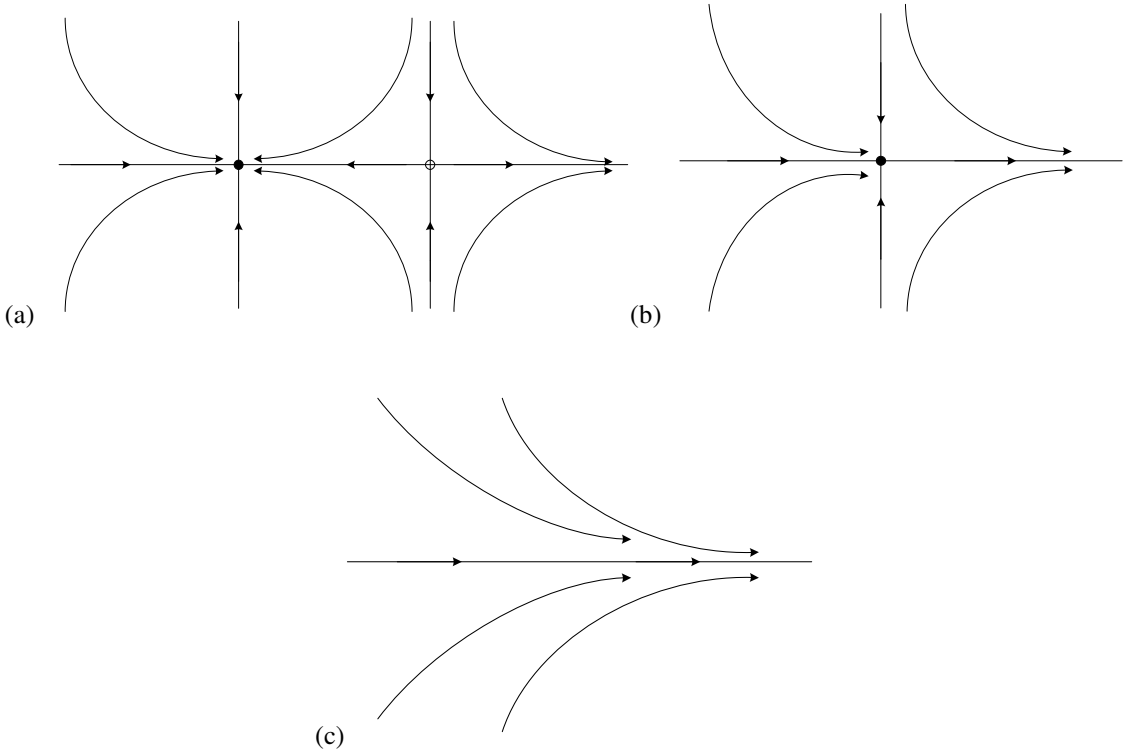

Figure 2.1. The saddle node (fold) bifurcation, shown for a planar system. (a) A stable and saddle node gradually merge together to produce the phase portrait in (b). The unstable node vanishes, resulting in local instability near the ghost of the saddle node in (c).

In the two dimensional case, we can ascertain two types of saddle node bifurcations. The bifurcation described in Figure 2.2 may occur in systems where there is a stable limit cycle present (meaning another unstable equilibrium point resides inside the limit cycle region). However, in the

special case where the saddle and stable equilibria reside on the limit cycle itself, we have a saddle-node on invariant circle bifurcation (also known as a *SNIC*). The phase portrait of a SNIC is shown below. With respect to Hodgkin-Huxley models, SNICs are observed to vary spiking frequency but preserve amplitude by effectively "slowing down" the trajectory along the limit cycle as the bifurcation parameter approaches criticality (Izhikevich, 2007).

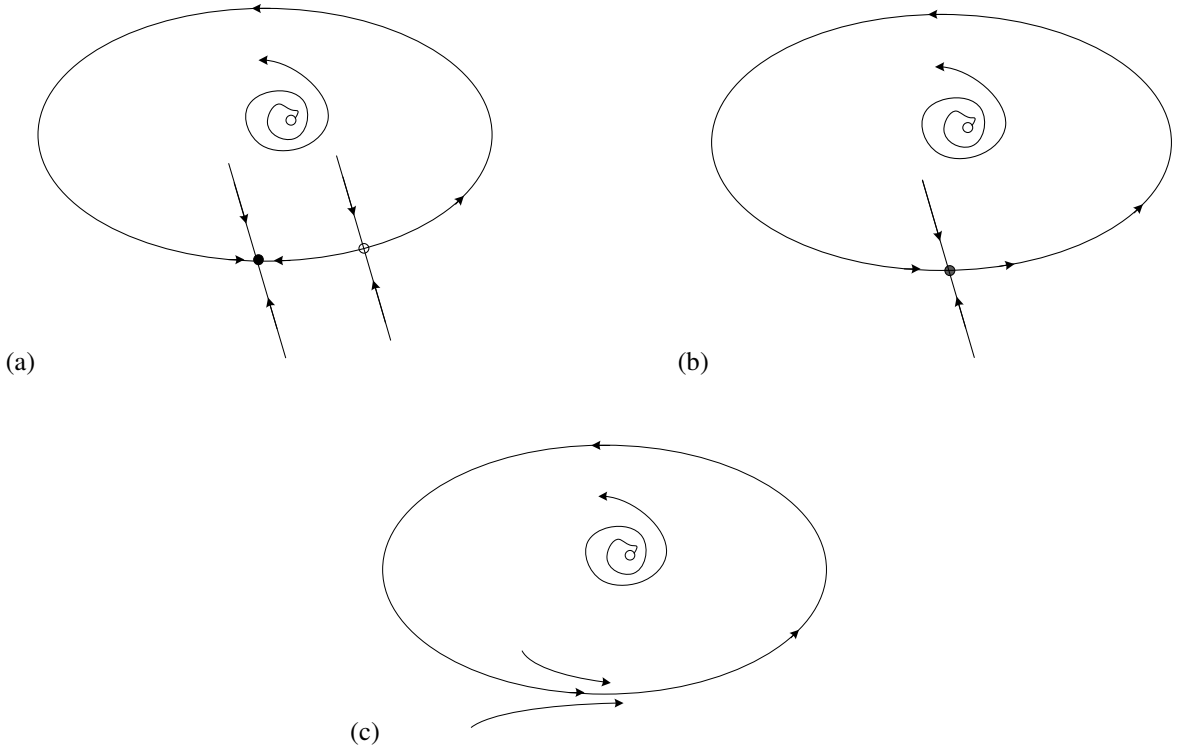

Figure 2.2. Saddle-node on invariant circle (SNIC) bifurcation. Similar to the saddle node bifurcation in Figure 2.1, a stable and saddle point converge reside on a limit cycle (a), converge, causing the stable equilibrium to lose stability (b) and eventually vanish, leaving only the stable limit cycle behind (c).

Andronov-Hopf Bifurcations

Andronov-Hopf bifurcations characterize a shift where a system's stable equilibrium point becomes unstable and gives rise to a stable limit cycle (supercritical case), or where a stable equilibrium point is surrounded by an unstable limit cycle which shrinks and collapses on it, making the equilibrium point unstable (subcritical case). In both cases, the eigenvalues take the form $a \pm bi$ with $a<0$. As $a=0$ and

the eigenvalues move across the complex plane, the focus loses stability (an example of this loss of stability is visible in Figure 1.2 for the Hindmarsh-Rose system). Figure 2.3 illustrates phase portraits of these bifurcations in progression.

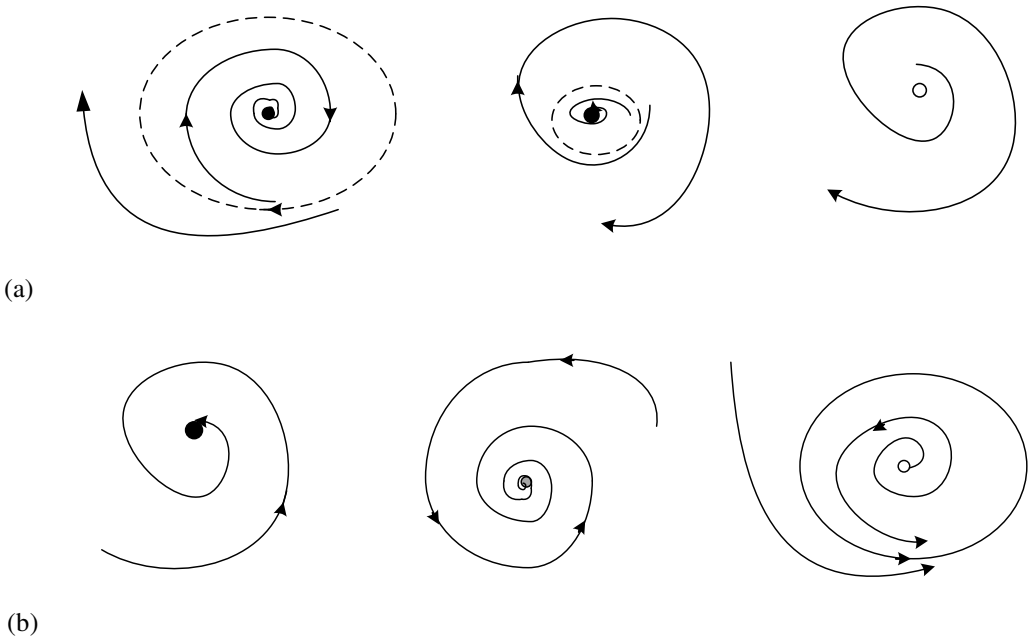

Figure 2.3. Andronov-Hopf bifurcations. (a) Sub-critical case: An unstable limit cycle collapses onto a stable focus to produce an unstable focus. (b) Super-critical case: A stable focus loses stability, giving rise to a stable limit cycle surrounding a now unstable focus.

A signature feature of the supercritical Andronov-Hopf bifurcation is the vanishing amplitude of the stable limit cycle as the bifurcation parameter approaches criticality.

Homoclinic Bifurcations

We first note that an orbit is termed *homoclinic* if it passes through both the unstable and stable manifolds of a saddle equilibrium. It is this feature that gives rise to the homoclinic bifurcation in the two-dimensional case. Recall that with saddle equilibria the eigenvalues λ_1, λ_2 are of opposite sign. For the homoclinic bifurcation with $\lambda_1 + \lambda_2 > 0$, a homoclinic trajectory emerges at the bifurcation point, and past the bifurcation point the stable fixed becomes surrounded by unstable limit cycle (Figure 2.4). In the

case where $\lambda_1 + \lambda_2 < 0$ (shown in Figure 2.5), the saddle persists, but instead a stable limit cycle converges with the homoclinic orbit and dissipates, leaving only the unstable equilibrium in Figure 2.5c.

In the supercritical case, we can observe the trajectory of the limit cycle move more slowly as it nears the saddle node; as the bifurcation parameter approaches criticality, the limit cycle period T increases logarithmically without bound until the limit cycle becomes a homoclinic trajectory.

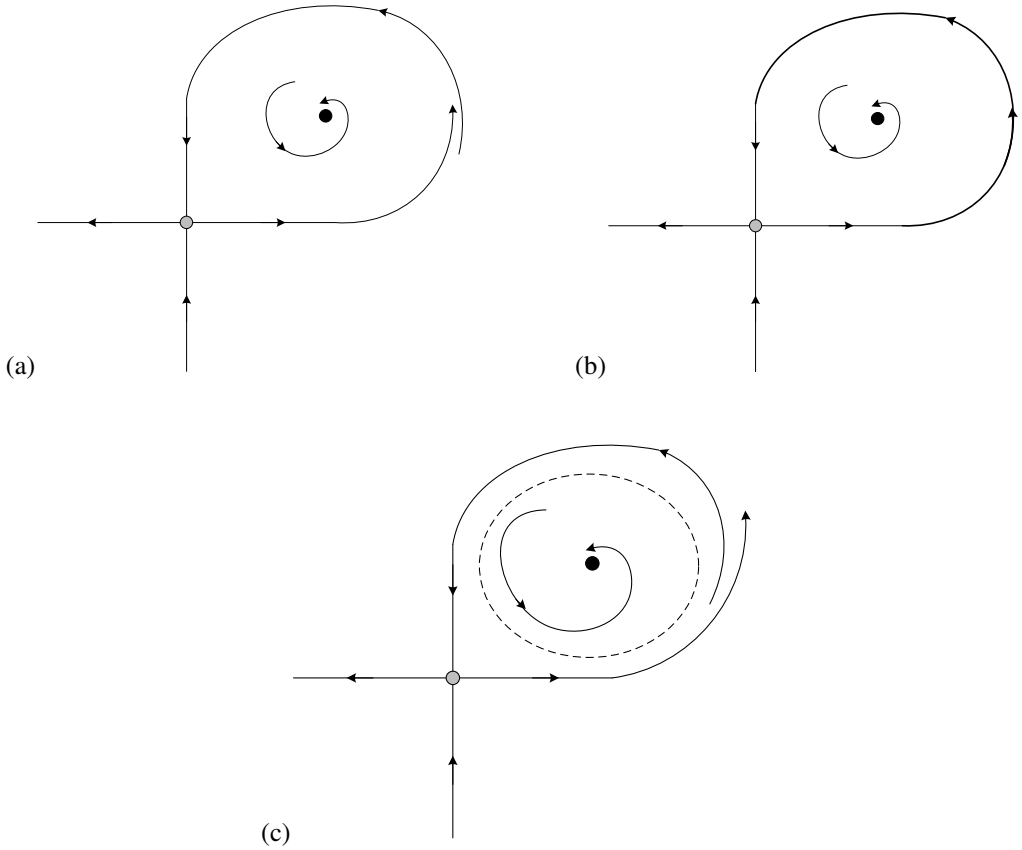

Figure 2.4. Homoclinic bifurcation, with $\lambda_1 + \lambda_2 > 0$. (a) The unstable manifold for the saddle node tends towards a stable focus; (b) The stable and unstable manifold for the saddle node intersect; this intersection is called the *homoclinic orbit*; (c) An unstable limit cycle appears, causing the unstable manifold to push trajectories onto the opposite side of the stable manifold.

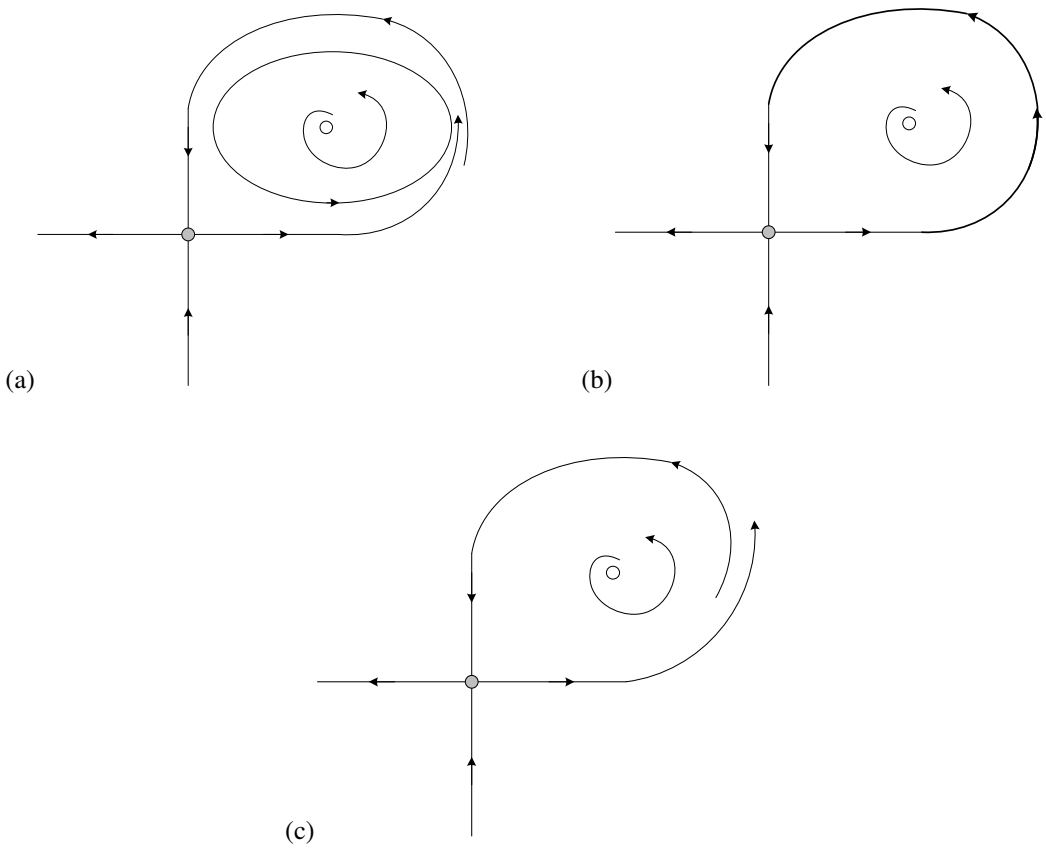

Figure 2.5. Homoclinic bifurcation, with $\lambda_1 + \lambda_2 < 0$. (a) The unstable manifold for the saddle node tends towards a stable limit cycle; (b) The homoclinic orbit appears at the point of bifurcation as a result of the limit cycle collapsing into the stable and unstable manifolds; (c) The limit cycle vanishes, leaving only an unstable focus; the unstable manifold pushes trajectories onto the opposite side of the stable manifold.

Synchronous Behavior in Networks

We now turn our attention to the characteristics of synchronization of neurons organized in small networks. In the case of a 2 cell neuronal network, neurons may be coupled with one another via inhibitory or excitatory synaptic couplings, introduced via a synaptic current I_{syn}. Each neuron may exhibit a burst period, which we denote by T_1 and T_2. We say that the two cells are *synchronized* if their voltage traces and their bursting periods are equal ($T_1 = T_2$). Neurons with equal bursting periods where bursting occurs at a constant phase shift Φ with respect to each other are said to be *out-of-phase* or *anti-phase*. In the case of $\Phi=0$ the neurons are said to be *in-phase.* In-phase synchronization can occur in a

non-identical form, where bursts are sufficiently close to each other but the spike trains are non-identical, as well as complete synchrony, where burst trajectories become identical. The trivial complete synchronization case is when the synaptic coupling current is absent and the neurons are effectively not interacting with each other. Lastly, we mention the *desynchronized* scenario, where bursting neurons do not settle to a particular bursting rhythm with respect to each other over an indefinite time period.

In order to achieve and analyze burst synchronization, we have limited means of manipulating neurons that are applicable to a real-world scenario. In effect, we only have the external applied current, which is reported to produce different synchronization outcomes between clusters of differently configured neurons (Terman, et al, 2002). In addition to being subjected to variable external currents, neurons may also be *phase shifted* with each other, meaning that they represent a different state along the same orbit at the same time. For instance, consider 2 uncoupled neurons that are firing and emitting the same burst pattern. If we take points along the burst orbit at time t for each neuron, the "position" or state of each neuron is regarded as its phase with respect to another neuron, Φ (Figure 2.6). To produce this phase shift artificially, we effectively "lock down" the neuron for a fixed length of time by setting the synaptic coupling current to zero. By doing this, the neuronal network operates and behaves as if the impacted neuron is not present in the network. After the lockdown period has passed, the neuron resumes participation in the network. At this point, the neuron may be out of phase with respect to the other neurons in the network whose voltage trajectories will be at different stages of their respective periodic orbits.

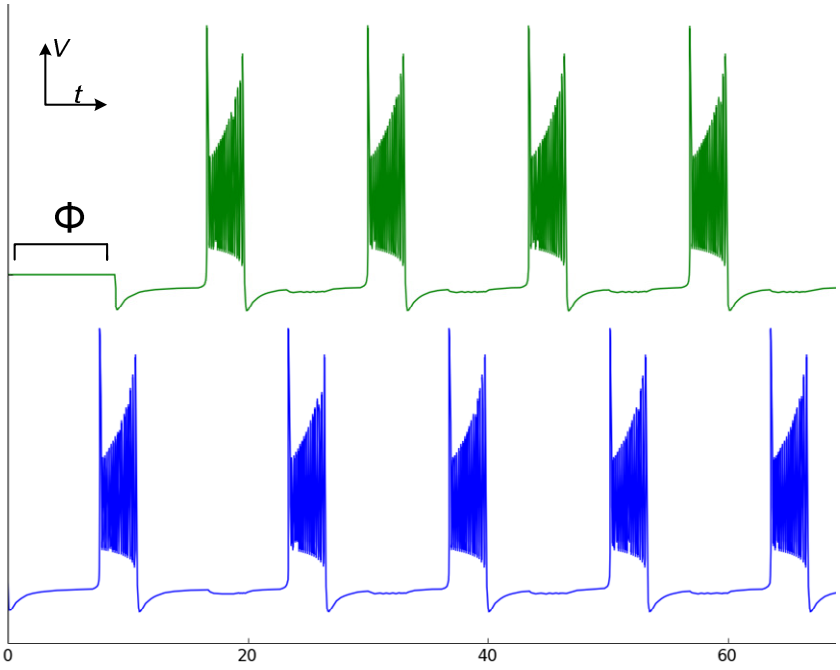

Figure 2.6. Phase shift between two neurons.

Half Center Oscillators

One of the simplest neuronal networks commonly found is the half-center oscillator (HCO). The HCO has been identified in a variety of neuroscience literature as a driver for multifunctional behaviors within central pattern generators (CPGs) (Shilnikov, et al., 2008). In the HCO, both neurons pass inhibitory currents to each other, preventing its counterpart from firing action potentials. In the case when the neurons are configured similarly and exhibit bursting, the inhibitory signal causes one neuron to be "locked down" until the initiating neuron undergoes bifurcation from bursting to quiescence, allowing its counterpart to be released and transition from quiescence to bursting. This mechanism is illustrated below for the leech heart interneuron in Figure 2.7. We note that this particular mechanism is only successful in regions where the neuron can enter bursting modes; in the case of tonic spiking, one neuron will lock down the other permanently, never allowing it to produce action potentials (Shilnikov, et. al, 2008).

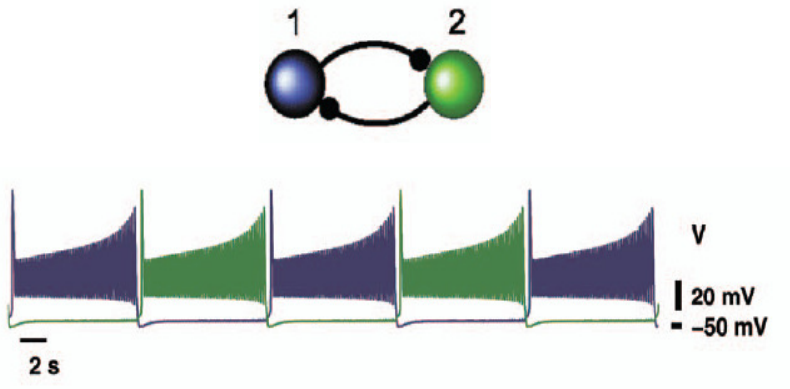

Figure 2.7. The half-center oscillator (modified from Shilnikov, et al., 2008).

HCOs do not just manifest anti-phase behavior; it has been found that by varying the activation gating parameters in a Hodgkin-Huxley model, full synchronization can be achieved between inhibitory bursters (Jalil, et al. 2009). Moreover, this synchronization appears to be robust within the HCO, allowing for slight deviations between inhibitory coupling strengths of the two neurons.

If adjusting the coupling strength of the system is sufficient to alter the bursting pattern produced by neuronal networks, it is also possible that bifurcations can also produce shifts in burst rhythms. Certainly one given example is adjusting the bifurcation parameter V_{K2}^{shift} (described in more detail in §3) in the leech heart interneuron below the bifurcation point, increasing the duty cycle of the burst until tonic spiking is present, thus locking down the other neuron in the oscillator. As the system approaches a homoclinic saddle node bifurcation, the burst duration increases and affects the overall network period of the HCO. Our choice of V_{K2}^{shift} allows us to configure the length of the burst accordingly.

Multistability and Polyrhythmicity

We conclude our discussion with a characterization of multistable states in neuronal networks with more than two cells. For the Hodgkin-Huxley model of a single neuron we can express the synaptic current I_{syn} as

$$I_{syn} = I_{syn}^{inh} + I_{syn}^{exc}$$

where

$$I = g_{ij}s(E - V_i)$$

is a current that can be either excitatory or inhibitory, with *s(t)* denoting a square-wave pulse function indicating when the current is switched on or off for a specific time interval. We note that the synaptic coupling strengths may vary between pairs of neurons in the network, therefore we may refer to each coupling strength between neurons *i* and *j* as g_{ij}. Additionally, the equation above also assumes instantaneous synaptic firing; we can apply non-instantaneous kinetics to the current by introducing a sigmoidal function as follows:

$$I = g_{ij}s(E - V_i)\Gamma(V_i)$$

$$\Gamma(V_i) = \frac{1}{1 + \exp\left[-1000\left(V_i - \Theta_{syn}\right)\right]}$$

The term Θ_{syn} corresponds to the bursting threshold of the membrane, i.e. the voltage at which the synaptic current becomes active, and *E* as before corresponds to the reversal potential. The actual value for the reversal potential may differ between inhibitory and excitatory currents.

By establishing a model for these currents in individual neurons, we can begin to connect them together to form simple, small scale neuronal networks much like the half-center oscillator. Such networks are referred to as *motifs*; similar to the half-center oscillator, motifs are regarded as the building blocks of central pattern generators (CPGs) that play a significant role in multifunctional behaviors. Motifs of just three cells can produce a wide variety of bursting patterns depending on the initial burst order and introduction of external perturbations, a phenomenon known as *multistability*. Motif structures associated with this have been readily identified, for instance, in neuronal pathways of the nematode *C. elegans*, in mammalian cortices of rats (Sporns, et al., 2004), and of course the CPG responsible leech

heartbeat. Additionally, motifs are classified into structural and functional configurations (Sporns, et al., 2004); we consider the latter only, where all three participants in the motif must exhibit some type of connection to each other. Since motifs may contain a mixture of inhibitory and excitatory synaptic currents, there potentially exists a degree of complexity to the basins of attraction that correspond to burst outcomes.

Typically, in any three cell motif we may have one of the following attracting outcomes when the neurons begin bursting and passing inhibitory or excitatory signals over the network.

Table 2.2. Categorization of burst rhythm patterns.

Outcome	Activity
Case I In phase synchrony	All neurons are in bursting in phase, and cannot inhibit each other from bursting. The network period is the same as the burst period.
Case II Single-winner dynamics	One neuron bursts out of phase with respect to each other. The network period remains constant, signifying that the bursts are synchronized. The out of phase neuron will lock down the other two neurons until is burst is complete. In this scenario the "winning" neuron is known as the *pacemaker* neuron. With the introduction of external perturbations such as hyperpolarizing current, it is possible to force the pacemaker role to pass from one neuron to another (Shilnikov, et al., 2008).
Case III Winnerless dynamics	All neurons burst out of phase with respect to each other. The network period is increased but remains constant. There are two possible cyclic burst order scenarios: Blue-Green-Red and Blue-Red-Green, which correspond to counterclockwise and clockwise bursting patterns respectively.

For the motif example in Figure 2.8 below, and thereafter through the course of the work, we denote the neurons by color: neuron 1 = "blue", neuron 2 = "green", and neuron 3 = "red". It is certainly possible that by applying external perturbations to the motif the outcome can be shifted from one particular outcome to another (Shilnikov, et al., 2008). The question, and in fact the question posed by this work, is to understand which shifts applied to the network result in changes to the attracting states of the network and which states act as unstable repellers in the system.

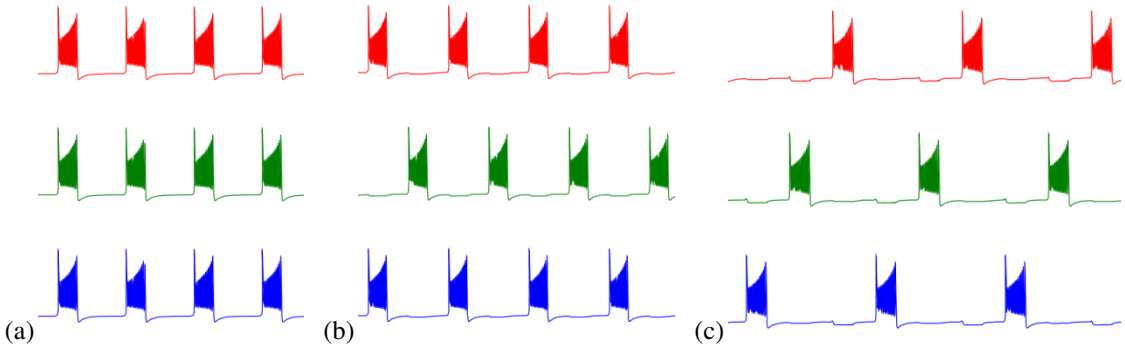

Figure 2.8. Burst outcomes in a three cell motif. (a) global synchrony; (b) single winner dynamics; (c) winnerless dynamics.

3. MODEL CHARACTERISTICS AND METHODOLOGY

The Leech Heart Interneuron

Our principal focus for this work is the Hodgkin-Huxley representation of the leech heart interneuron. The interneurons are coupled in an inhibitory fashion in a leech to produce a pattern generator responsible for leech heartbeat activity (Cymbalyuk, et al., 2002). The model is empirically derived in part by applying a series of voltage clamp experiments, a process where the membrane potential is kept constant while current is passed to the membrane and measured when the monitored potential equals the membrane potential (Cymbalyuk, et al. 2005). The measurement of this relationship between instantaneous current and voltage yields curves for activation gating parameters. The model is shown here in its pharmacologically reduced form, along with a table of fixed parameters in Table 3.1.

$$C\frac{dV_i}{dt} = -(I_{Na} + I_{K2} + I_{leak} + I_{pol} + I_{syn})$$

$$\tau_{Na}\frac{dh_i}{dt} = f(500, 0.026 + \sigma_h, V_i) - h_i;$$

$$\tau_{K2}\frac{dm_i}{dt} = f(-83, 0.018 + V_{K2}^{shift}, V_i) - m_i$$

$$I_{Na} = g_{Na} f(-150, 0.27 + \sigma_n, V_i)^3 h_i (V_i - E_{Na});$$

$$I_{K2} = g_{K2} m_i^2 (V_i - E_K);$$

$$I_{leak} = g_{leak}(V_i - E_{leak})$$

$$I_{syn} = -\sum_{j=1}^{n}\left[g_{ij}^{in}(E_{syn}^{in} - V_i) + g_{ij}^{exc}(E_{syn}^{exc} - V_i)\right]s(t)\Gamma(V_j - \Theta_{syn})$$

$$f(a, b, V) = \frac{1}{1 + \exp\left[-a(V + b)\right]}$$

$$\Gamma(V_i) = \frac{1}{1 + \exp\left[-1000\left(V_i - \Theta_{syn}\right)\right]}$$

where:

V_i is the membrane potential,

I_{Na} is the sodium current,

I_K is the potassium current,

I_{leak} is the leak current,

I_{pol} is the polarization current,

I_{syn} is the synaptic current,

g_{ij} is synaptic coupling strength between neurons i and j,

s(t) is a square-wave pulse function using H(t) for a specific time interval $[t_{on},t_{off}]$, signaling whether I_{syn} is active or not.

$\mathbf{\Gamma}$ is the sigmoid function used to drive inhibitory synaptic coupling between neurons.

We create a three cell inhibitory motif using this model; hence i corresponds to the i-th neuron in the motif. The slow-fast system above contains two time scales, incorporating a fast K^+ current and a slow persistent Na^+ current. The original model, in its comprehensive form, would entail a 14 dimensional system of ODEs with 5 separate time scales; because of the complexity of the full system, we reduce the system pharmacologically, taking into account only the primary ionic currents and their associated gating variables. These currents are of particular importance to us and their (in)activation strongly influences the synchronization outcomes we are studying (Jalil, et al, 2009; Shilnikov, 2008); the other currents are assumed to either be instantaneous or absent from the model altogether. Lastly, it is noted that we introduce an external applied current I_{pol}, a non-variable current produced by latent activity between neurons organized in the motif.

Table 3.1. Parameter settings for the leech heart interneuron.

Parameter/Value	Description
$C = 0.5$	Membrane capacitance, μF
$G_{K2} = 30$	K^+ maximal conductance, nS/μm2
$E_K = -0.07$	K^+ reversal potential, V
$E_{Na} = 0.045$	Na^+ reversal potential, V
$G_{Na} = 160$	Na^+ maximal conductance, nS/μm2
$G_l = 8$	leak maximal conductance, nS/μm2
$E_l = -0.046$	leak reversal potential, V
$I_{pol} = 0.006$	polarization current, mA
$\sigma_m = 0.0035$	fixed gating parameter
$\sigma_h = 0.0065$	fixed gating parameter
$\tau_{K2} = 0.9$	K time constant
$\tau_{Na} = 0.0405$	Na time constant
$E_{syn} = -0.0625$	inhibitory reversal potential, V
$\Theta_{syn} = -0.03$	Synaptic threshold, V
$n = 0.018$	Gating parameter for activation of I_K
$h = 0.99$	Gating parameter for inactivation of I_{na}

Several other considerations should be noted about the system above:

- For our purposes the excitatory coupling strengths $g^{exc}=0$ for all neurons in the motif.
- The motif is strictly driven by inhibitory signals, which are varied in strength.
- All neurons in the motif are configured identically based on the parameters in Table 3.1.
- In addition to phase shifts for each instance of the model, V_{K2}^{shift} is adjusted to account for the strength of the burst in order to obtain specific bursting dynamics. V_{K2}^{shift} is equal for all neurons in the motif.

Stability Analysis of an Isolated Neuron

We provide a cursory discussion of the stability analysis of a standalone leech heart interneuron; it is necessary to examine behaviors that may shift stability in an individual neuron in order to understand how inhibitory current applied at a specific phase of a burst cycle will impact synchronization outcomes.

Bifurcations occurring in the reduced system have been reported on extensively (Shilnikov, et al., 2004, Cymbalyuk, et al. 2005).

Figure 3.1 shows a bifurcation diagram with V_{K2}^{shift} as the bifurcation parameter, and varying levels of (constant) synaptic current introduced to the neuron. The leech heart interneuron is a principal example of a *square wave burster*, a system which undergoes a saddle node bifurcation when transitioning from quiescence to bursting, and a homoclinic saddle node bifurcation when transition from bursting back to quiescence (Rinzel, 1987). Figure 3.2 depicts this activity as the burst trajectory moves along the nullcline's stable branch until the saddle node bifurcation is reached, at which point the trajectory moves onto the stable manifold surrounding the upper branch of the nullcline. The trajectory gradually moves forward, but the stable manifold coincides with the unstable branch of the nullcline, thus giving rise to the homoclinic bifurcation, and the trajectory returns to the stable branch. This loop is repeated as long as the value of V_{K2}^{shift} permits bursting activity.

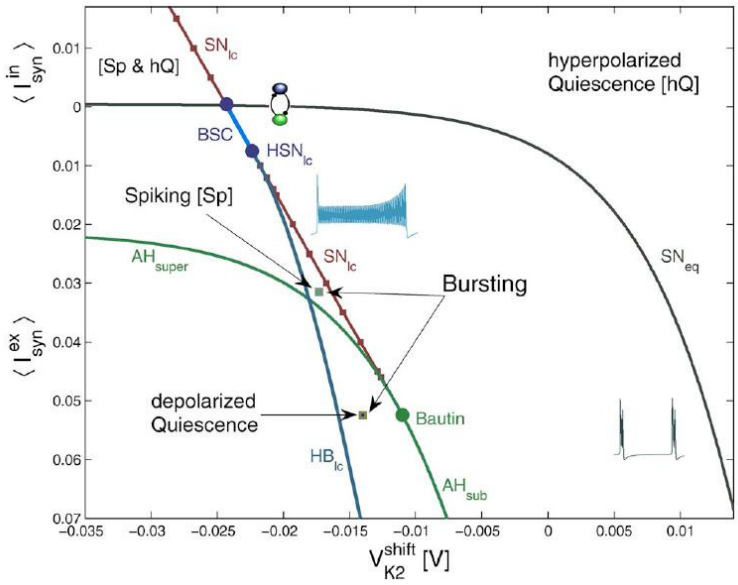

Figure 3.1. Bifurcation diagram for the leech heart interneuron. The bifurcation boundaries partition the V_{K2}^{shift}-I plane into regions of bursting, tonic spiking, and quiescence, with a small intersected region where bistability is present (taken from Shilnikov, et al., 2008).

V_{K2}^{shift} allows us to adjust the slow nullcline m′=0, shaping the length of the burst; by slowing the K^+ activation current the burst duration can be increased. Below $V_{K2}^{shift} \approx -0.024$ only tonic spiking or quiescent states can exist, meaning that should the neuron go into tonic spiking, the burst trajectory will stay on the stable manifold and be unable to return to the stable branch of the fast nullcline (Shilnikov, et al. 2005).

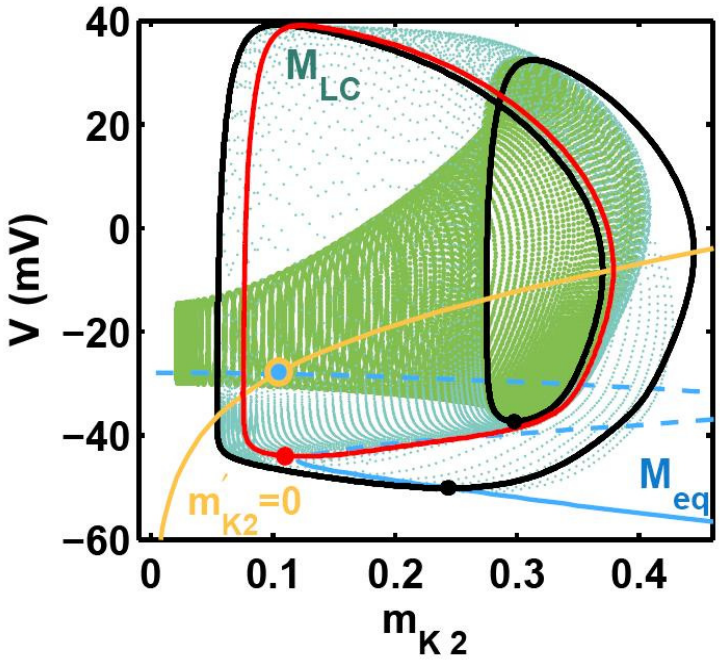

Figure 3.2. Burst diagram for the leech heart interneuron. The slow nullcline m′=0 intersection with the stable manifold is determined by the bifurcation parameter V_{K2}^{shift}. The burst trajectory moves from quiescence (lower branch of the fast nullcline) via saddle node bifurcation onto the manifold M_{lc}, producing spiking activity until terminating via a homoclinic bifurcation as M_{lc} intersects the unstable branch of the fast nullcline (taken from Channell, et al., 2007).

It should be noted however, that there exists a small region reported to exhibit bistability; that is, both tonic spiking and bursting modes can be exhibited by the neuron (Cymbalyuk, et al., 2005). This coexistence is created by observing two things: 1) bursting occurs between saddle node bifurcation of the equilibrium point and a homoclinic bifurcation of the limit cycle that corresponds to the actual burst; 2) tonic spiking occurs between saddle node bifurcation of the equilibrium point and an Andronov-Hopf

bifurcation that occurs along the depolarized branch of the nullcline. The intersection of these two basins of attraction yields a reduced region where both modes may coexist. Moreover, it is possible to introduce a transition between the two modes by causing a saddle node periodic orbit to appear within the stable limit cycles produced along the stable manifold; this transition between tonic, non-transient spiking and burst modes is known as a *blue sky catastrophe* (Shilnikov, 2004).

In summary, we must confine our neurons to use specific values of V_{K2}^{shift} in order to produce the desired bursting, but we may also adjust the V_{K2}^{shift} values in order to bring us closer to a specific bifurcation or cusp where stability shifts are imminent and measure changes in synchronization outcomes.

Inhibitory Ring Networks

The arrangement of leech heart interneurons in a motif is fairly straightforward. We consider two types of inhibitory motifs: strongly coupled, where g_{ij} are relatively large, and synchronization is rapid; and weakly coupled, where $g_{ij} << 1$ and synchronization patterns may be observed over a large number of burst cycles or not at all. Additionally, we also consider asymmetric as well as symmetric inhibition (Figure 3.3), the former set up so that values of g_{ij} are significantly stronger in one direction. For the purposes of this study, for all asymmetric measurements are assumed to be in the clockwise direction.

Considering the networks in Figure 3.3, there exists two possible burst cycles. For uncoupled neurons ($g_{ij}=0$ for all i,j), the duration of the neuron's burst cycle, or period, is said to be *isolated* (denoted by T_{iso}), since no synaptic current is being injected or output from any neuron to its neighbors. For non-zero g_{ij}, we have what is considered to be the *coupled* burst cycle between neurons i and j, whose period is denoted by T_{coup}. In general, because of the presence of synaptic current, the burst period is altered, and $T_{iso} \neq T_{coup}$ (Figure 3.5). It should also be noted that the inhibitory motif also has a relative network period (the duration which the entire burst pattern is completed by the network), generally with a minimum of T_{coup}, but increases for single winner and winnerless burst outcomes.

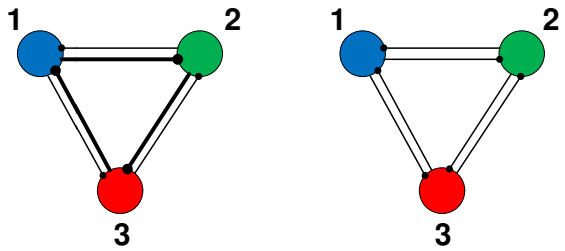

Figure 3.3. Asymmetric and symmetric inhibitory motifs. For the asymmetric case biased synaptic coupling is oriented in the clockwise direction.

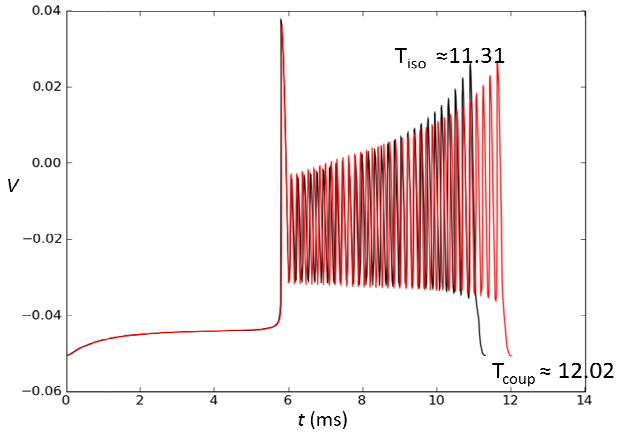

Figure 3.4. Isolated and coupled network periods T_{iso} and T_{coup}. Synaptic coupling between cells causes the burst duration to increase.

Setup of Phase Shift Analysis

One of our principal investigations is centered on the impact of phase shifting on multistable states in our three cell inhibitory motif described previously. Below we discuss some of the methodology applied towards evaluating the basins of attraction produced by three oscillators; previous processes used to evaluate the parametric phases of coupled oscillators have been considered for networks of three and four cells (Ashwin, et al., 2008; Canavier, et al. 1999) and the approach used here is similar. Consider the inhibitory rings in Figure 3.4. In the inhibitory motif setup, the outcome of bursting rhythms is dependent

on the burst duration as well as the relative phase shift between cells as described in §2. With respect to a particular neuron in the motif, the other two neurons may be initiate bursting at different phase shifts Φ_1 and Φ_2; a third phrase shift is not necessary since it would be directly computed from the first two phase shifts. We begin by locking down neuron 1; here no delay is ever introduced to this neuron, and we introduce a pair of phase shifts (Φ_1, Φ_2) which reflect the duration of time that cells 2 and 3 are "off." The shifts are normalized with respect to the isolated period T_{iso}. For a specific length of time (measured in burst cycles), we allow the network to burst and make note of the final bursting pattern produced in the simulation, an example of which is shown in Figure 3.5.

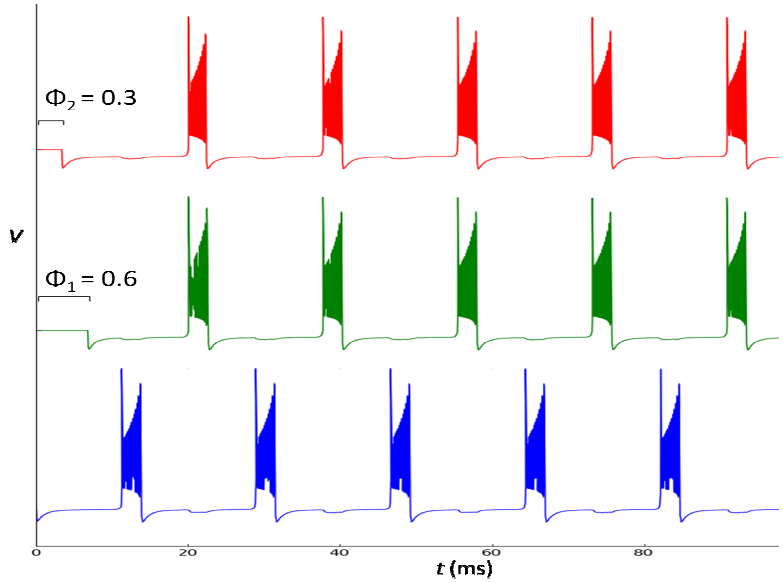

Figure 3.5. Example bursting rhythm with applied phase shift. Initial shifts (Φ_1, Φ_2) = (0.6, 0.3), are normalized with respect to T_{iso} In this scenario the outcome is single winner dynamics with red and green neurons in synchrony, and the blue neuron out of phase.

For our purposes, the excitatory coupling strengths g^{exc}=0. Excitatory coupling is not considered in the scope of this study. The motif is strictly driven by inhibitory signals, which are varied in strength, although all neurons in the motif are otherwise configured identically. Additionally, phase shifts are normalized with respect to T_{iso}. The motivation for this is that when non-zero shifts are applied, only one neuron is active, causing the coupled period to be the same as the isolated period.

Modeling and Data Analysis Tools

Several primary tools are used for modeling, analysis and visualization of results. They are covered briefly in terms of application.

Dynamic Solver

Developed by J. Aguirregabiria, dynamic solver is a system modeling tool for general ODEs. It is suitable for examining a single burster or an individual simulation of a small motif. Often, this trajectory data is captured and imported into other applications such as MATLAB for visualization.

PyDsTool

PyDsTool is an API of dynamical systems modeling utilities written by R. Clewley (2004). Developed in Python, scripts are written around the API in order to produce models of neuronal networks and other systems. The libraries are particularly used for collecting data based on the firing of neuronal events, such as spiking and bursting. Additionally, PyDsTool is used to compute an extremely accurate trajectory for an isolated neuron, which is applied as a set of initial points along a phase shifted orbit. For regular trajectories that are processed during a simulation of network activity, Dopri and Radau solvers are used.

Using PyDsTool, several simulation tools and data parsers were created in order to analyze and plot data produced as motifs are phase shifted. The output is written to data files as well as visualized using a suite of MATLAB libraries for Python.

With data collection mechanisms in place, we then set up a grid of values for (Φ_1, Φ_2) over which we perform phase shift simulations. In all cases, we normalize the phase shift (Φ_1, Φ_2) to be in the unit square $[0,1]x[0,1]$. Combinations of phase shifts are taken from this interval and applied to the motif. To do this we set step sizes for Φ_1 and Φ_2 over the unit interval: e.g., if $\Delta\Phi=0.01$, this produces 10000 data points. We use $\Delta\Phi=0.02$ for the bulk of our simulations; a lower step size is used only in refining

particular sub-regions of the unit interval, and higher step sizes are used for testing and performing consistency checks, where data are merely verified to see if the outcome match the expected result, given our configuration. We also note that for all simulations the burst threshold Θ_{syn} = -0.04; as the voltage trajectory passes this value, threshold events are fired to signify an action potential is imminent. In all cases, we record the relative phase, spike count, duty cycle, and relative network period with respect to T_{coup}.

For the strongly coupled motifs, we observe basins of attraction for bursting patterns as the strength of the synaptic inhibition in the clockwise direction is gradually increased. In the weakly coupled motifs, in addition to capturing the basins of attraction, we also parameterize Φ_1 and Φ_2 with respect to time and observe the traces as the two shifts evolve while the motif is active. In this case, the number of settle cycles is increased in order to observe longer traces in Φ_1x Φ_2. The resulting equilibria states correspond to bursting patterns, including repeller states whose burst configurations are not converged to by phase shifted motifs.

4. RESULTS

We report our results as data are collected along two separate axes. Along one axis we examine the shifts between symmetric and asymmetric inhibitory motifs, where the synaptic coupling strength is increased in one direction, and along a separate axis we examine the qualitative characteristics distinguishing the behavior of strongly and weakly coupled motifs. Our ultimate aim is to interpret the bifurcations and shifting basins of attraction that result by applying these changes to the three cell motif. Table 4.1 below provides a brief description of the procedures carried out for each combination of symmetry and coupling type.

Table 4.1. Classification of results for inhibitory motifs.

	Strong Coupling	**Weak Coupling**
Symmetric	Coupling strength g is constant in both directions. Phase shift basins of attraction are computed.	Coupling strength g is constant in both directions. Values of $g << 1$. Phase shift basins of attraction and phase portraits are computed. V_{K2}^{shift} is decreased. Phase portraits are computed to observe bifurcations that may result.
Asymmetric	Coupling strength g is increased unidirectionally towards 1. Phase shift basins of attraction are computed.	Coupling strength of g is increased unidirectionally. Values of $g << 1$. Phase portraits are computed to observe bifurcations that may result.

Strongly Coupled Motifs: Symmetric Cases

For the fully symmetric case, we compute burst rhythm outcomes for discretized values of phase pairs (Φ_1, Φ_2) with Φ_1, Φ_2 in [0,1] . Figure 4.1 depicts the results for the symmetric strongly coupled case, with $g_{ij} = 0.1$, for all i,j, $V_{K2}^{shift} = -0.02$, and the number of settle cycles for the motif fixed at 10. As shown, there are three distinct basins of attraction that correspond to different bursting patterns, depending on the initial phase shift conditions. As the phases are varied with respect to T_{iso}, the resulting

burst rhythm shifts; one cell in the motif is always anti-phase with the other two, corresponding to single winner dynamics. The annotated regions below indicate which of the neuron is out of phase; 1, 2, and 3 correspond to blue, green, and red neurons respectively.

Each basin of attraction corresponds to following outcomes once the network has approached its asymptotic periodic cycle (which we will refer to as *settling*): Blue region: $(\Phi_1, \Phi_2) = (0.5, 0.5)$. Green region: $(\Phi_1, \Phi_2) = (0.5, 0)$. Red region: $(\Phi_1, \Phi_2) = (0, 0.5)$. To interpret this for the green region, for instance, we are saying that after the network has been active for a sufficient number of settle cycles, the blue neuron is out of phase from the green neuron by $0.5*T_{iso}$, and that the blue neuron is in phase with the red neuron . The other bursting outcomes can be read similarly. In any case, for the strongly coupled scenarios, convergence to each outcome is rapid, typically after the first burst cycle completes. Convergence to one of these patterns occurs regardless of our choice of (Φ_1,Φ_2), excepting $(\Phi_1,\Phi_2)=(0,0)$, when no phase shift exists between the neurons. Figure 4.2 (a-c) depicts samples of some of the burst outcomes with respect to the three basins of attraction.

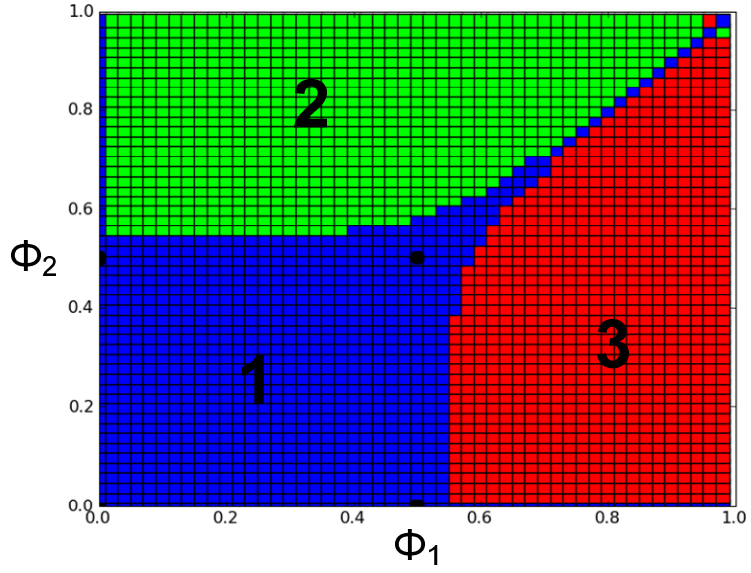

Figure 4.1. Phase shift plot for the strongly coupled symmetric case ($g_{ij} = 0.1$; $\Delta\Phi=0.02$). The three regions correspond to basins of attractions for the blue, green, and red neurons. The actual equilibria states, corresponding to the final burst pattern of the motif, are marked in black.

Strongly Coupled Motifs: Asymmetric Cases

For strongly coupled asymmetric cases, inhibitory coupling strengths are fixed in the counterclockwise direction for $g^- = \{g_{21}, g_{32}, g_{13}\}$, while the clockwise couplings $g^+ = \{g_{12}, g_{23}, g_{31}\}$ are varied identically in increasing magnitude from 0.1 to 0.9. The changes in the basin boundaries are minute and subtle as g^+ increases towards 0.6. The green region expands slightly and becomes more distorted but noticeably remains on the left side of the line $\Phi_1 = \Phi_2$, while the red basin of attraction contracts slightly. These burst regimes exhibit subtle distortions until $g^+ \approx 0.66$, where a sub-region suddenly appears in the green burst rhythm region, and continues to expand until it becomes tangent to the line $\Phi_1 = \Phi_2$ (Figure 4.4e). At $g^+ = 0.69$, another region appears, and this process cascades at an increasing rate until $g^+ = 0.70048$, when the bounded region above the diagonal appears to exhibit chaotic burst outcomes with respect to our choice of Φ_1 or Φ_2. The transition from randomized burst outcomes

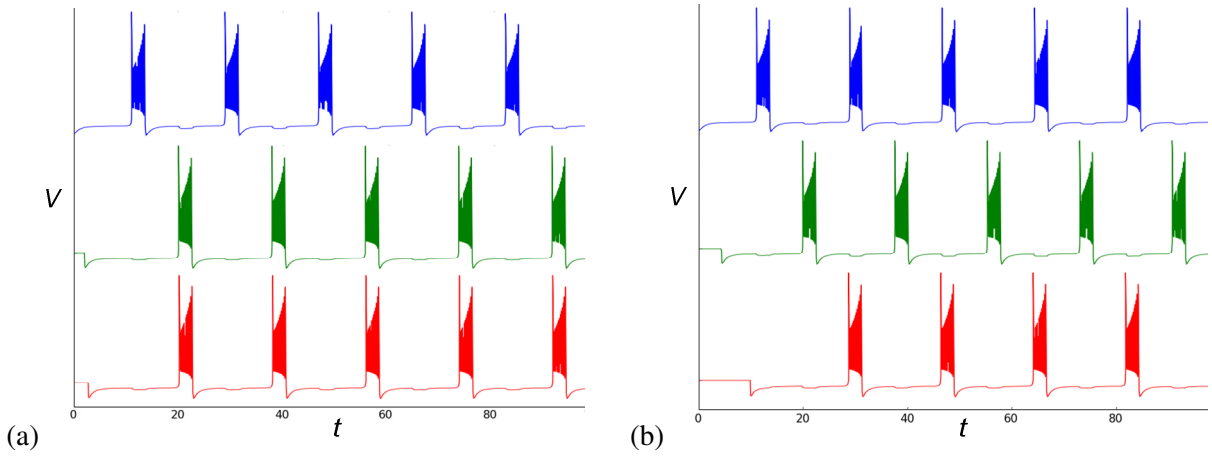

Figure 4.2. Burst patterns in the symmetric case ($g_{ij} = 0.1$). (a) $(\Phi_1,\Phi_2) = (0.2,0.25)$; (b) $(\Phi_1,\Phi_2) = (0.4,0.9)$.

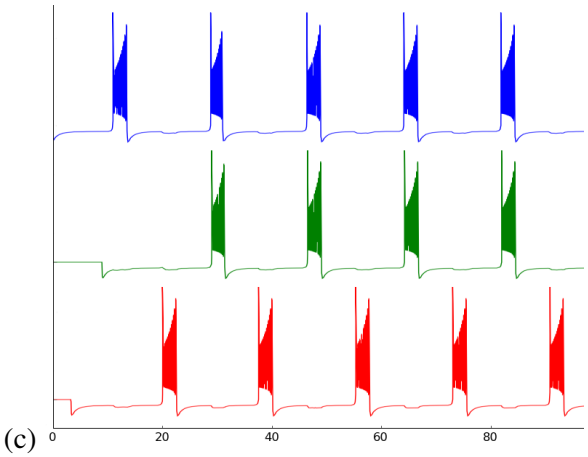

Figure 4.2, cont'd. Burst patterns in the symmetric case (g_{ij} = 0.1). (c) (Φ_1,Φ_2) = (0.8,0.3).

to desynchronized burst rhythms is extremely rapid, and dissimilar to the previous cascade of expanding regions described previously. In this case pockets of winnerless state outcomes begin to appear (Figure 4.4h) until all of the outcomes in the region become winnerless as g^+ is increased very slightly (Figure 4.4i). It should be noted that because of the sheer sensitivity of the value for g^+ as the transition between cascading regions of single winner bursting outcomes and the singular region of winnerless states, the number of settle cycles is adjusted upwards of 25 to verify that the strength of the coupling is still persistent even near this type of transition and produces the same outcomes.

Beyond this value for g^+, the new region begins to expand, as other previously single winner states begin to transition to winnerless ones. In this region the initial phase shift conditions (Φ_1, Φ_2) approach (0.333, 0.666) as the network settles. An example of this outcome is illustrated in Figure 4.3. As g^+ continues to increase, the original red, green, and blue basins of attraction become enveloped by a globally out of phase regime. By g^+=0.78 the winnerless state outcome occurs everywhere for all phase shifts.

The sequence of diagrams in Figure 4.4 on the following pages illustrate the basins of attraction producing sub-regions that yield a different burst outcome; this cascading behavior increases rapidly as g^-

approaches 0.7, at which point a new burst regime begins to appear. The final diagrams depict the transition to a globally out of phase burst outcome, regardless of our choice for (Φ_1, Φ_2).

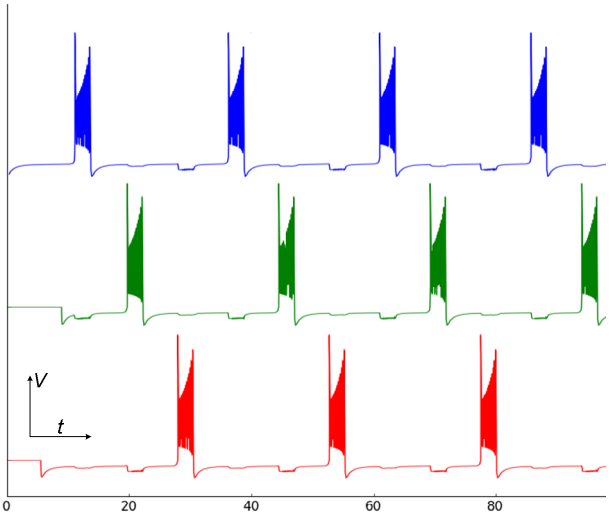

Figure 4.3. Example of a winnerless state burst outcome, for g^{-}=0.8; (Φ_1,Φ_2) = (0.8,0.5).

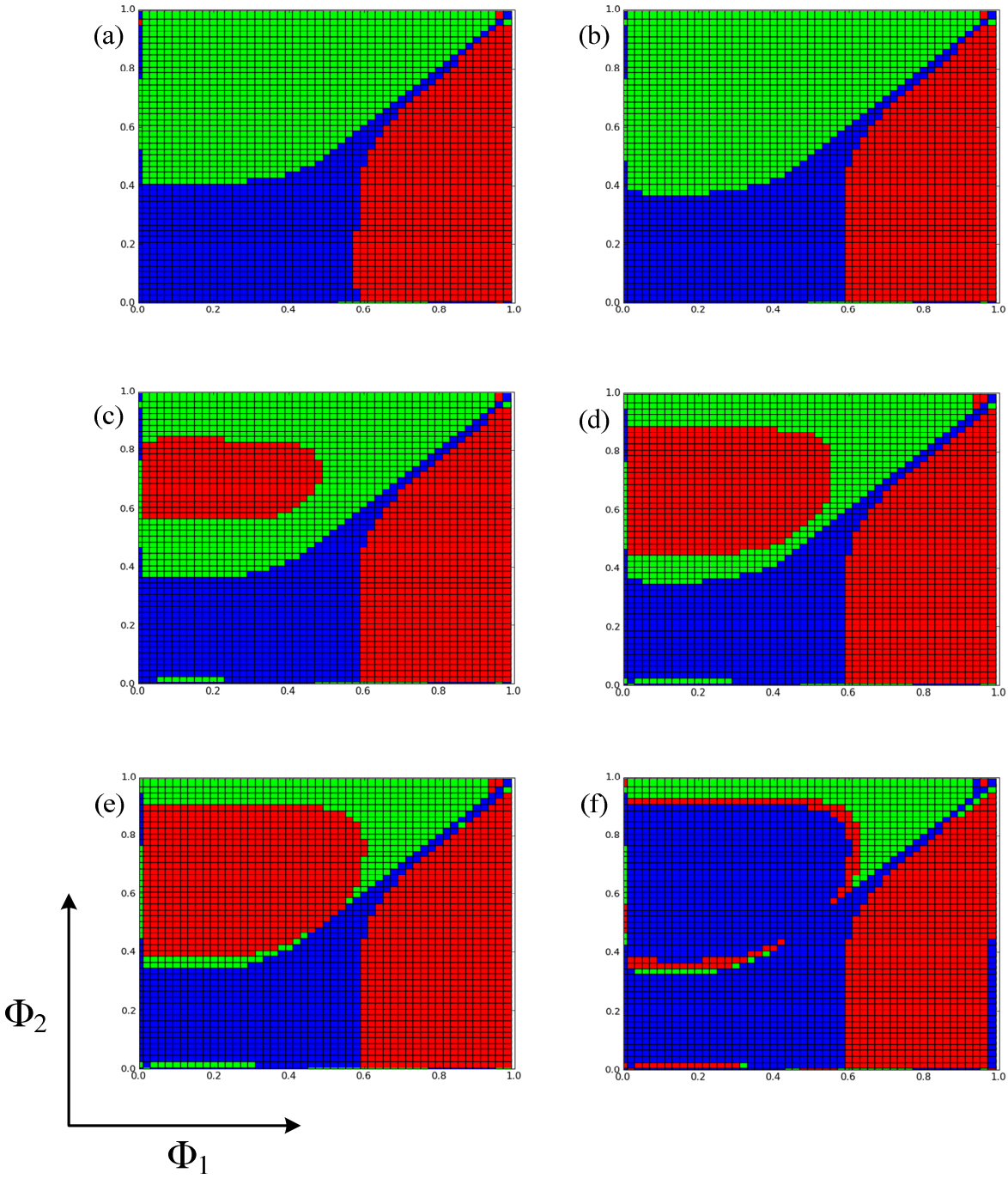

Figure 4.4. (insets a-f) Phase shift diagrams for the asymmetric strongly coupled motif, as g^+ is increased between 0.60 and 0.76. The symmetric basins of attraction relatively present in the strongly coupled case begin to show visible indicators of distortion at g^+=0.6. Cascading regions of shifting single winner bursting rhythms appear until the outcomes become chaotic as g^+ approaches 0.70. (a) g^+=0.6; (b) g^+=0.65; (c) g^+=0.66; (d) g^+=0.67; (e) g^+=0.68; (f) g^+=0.69.

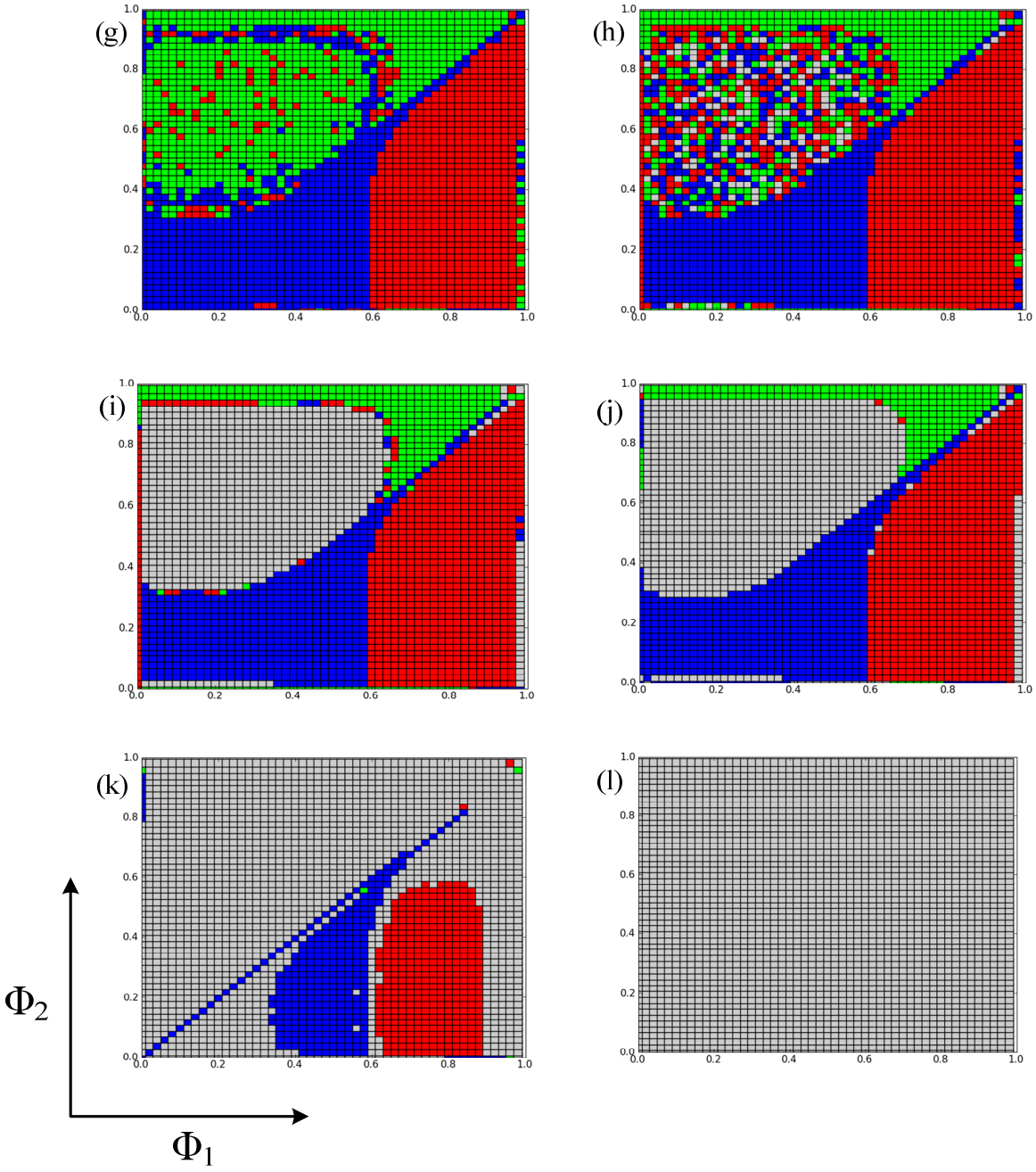

Figure 4.4, cont'd. (insets g-l) Around $g^+ \approx 0.70$ the cascading of single winner burst regimes gives way to chaotic outcomes, although the convergence to those outcomes remains consistently fast. Between $g^+=0.7004$ and $g^+=0.7006$ a region of winnerless states (insets h,i) rapidly coalesces, and grows until the outcome occurs everywhere for all Φ_1, Φ_2. (g) $g^+=0.70$; (h) $g^+=0.700485$; (i) $g^+=0.70054$; (j) $g^+=0.71$; (k) $g^+=0.76$; (l) $g^+=0.78$.

We make an observation about the globally desynchronized (but still phase locked) case that results from having a sufficiently strong g^+ driving the motif. Prior to the transition around g^+=0.7, a bursting rhythm can converge to one of the three stable phase equilibria (1.0,0.5), (0.5,0.5), and (0.5,1.0), while repelling away from the unstable equilibrium (0,0) (indicating no phase shift applied). These three single winner states reside in their respective basins of attraction (colored in red, blue, and green, respectively). Between g^+=0.7 and g^+=0.78 the single winner attracting states co-exist with the winnerless attracting state (0.333,0.666), and after g^+=0.78 only the latter equilibrium remains (Figure 4.5). This winnerless state resides in the basin of attraction colored in gray, and corresponds to the burst order 1-2-3 (green-blue-red), which occurs everywhere in $\Phi_1 x \Phi_2$. The only other possible winnerless outcome, corresponding to (0.666, 0.333) and its burst order 1-3-2, does not occur and is considered a repeller within the system.

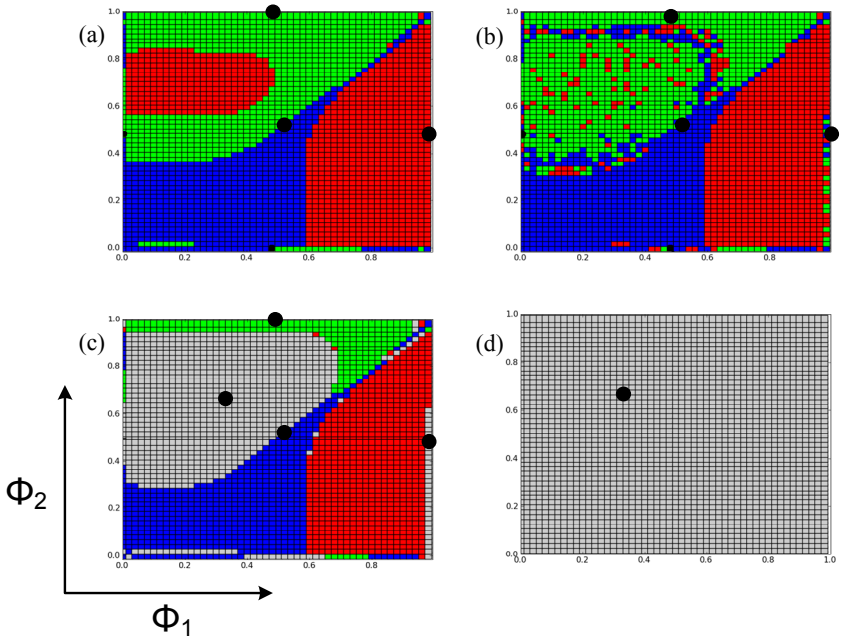

Figure 4.5. Transition between single winner stable equilibria to winnerless stable equilibrium states. Shown are phase shift diagrams annotated with the locations of the burst equilibria as g^+ is increased. (a) g^+=0.66; (b) g^+=0.70; (c) g^+=0.71; (l) g^+=0.78. The stable equilibria are shown in black.

Weakly Coupled Motifs: Symmetric Cases

Whereas strong coupling allows us to efficiently compute the basins of attraction with respect to the phase shifts (Φ_1, Φ_2), the convergence to burst outcomes is extremely rapid, and we are not easily able to ascertain the shifts in trajectories as the shift differences Φ_1, Φ_2 evolve through time. In the case of weakly coupled inhibition, burst rhythms take significantly longer to stabilize, but allow us to see the manner of convergence to the final burst pattern outcome. It is also important to note that because of weak coupling between neurons in the motif, the distribution of possible burst outcomes will appear different from that of the strongly coupled motifs.

Plotting the basins of attraction over the shift ranges [0,1]x[0,1] as before, we find that there exists well defined regions of both single winner and winnerless bursting states (Figure 4.6). Additionally, we qualify that in this case due to the presence of weak coupling, some of the initial phase shift conditions identified as yielding a winnerless state may in fact correspond to one of the other basins of attraction or be completely aperiodic due to the fixed number of settle cycles allotted for the motif. We also note that the basins of attraction for the weakly coupled case are markedly different in shape than those of the strongly coupled motifs.

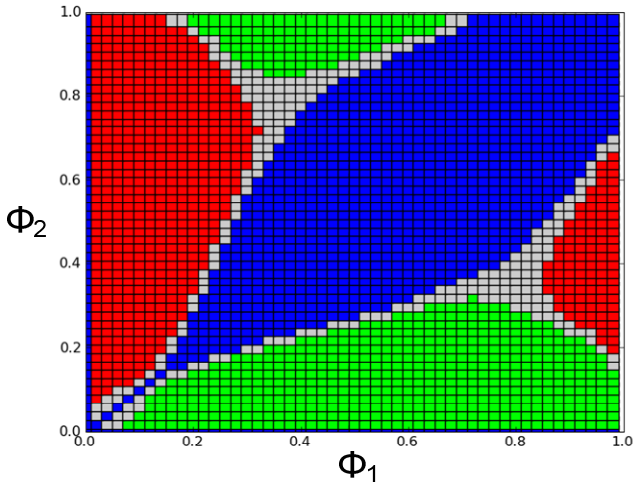

Figure 4.6. Phase shift diagram for the weakly coupled, symmetric motif (g_{ij} = 0.005; $\Delta\Phi$=0.02).

For the symmetric weak coupling case, we plot functions $\Phi_1(t)$, $\Phi_2(t)$, parameterized with respect to time t, indicating the relative phase difference between neuron pairs (blue, green) and (blue, red) respectively. This plot yields a phase portrait of the shifts which suggest possible mechanics of how the bursting rhythm arrives at a particular basin of attraction. In our initial setup, we fix $g_{ij} = 0.0005$ and raise the number of settle cycles to 25, allowing the motif significantly more time to settle. The following parameterized phase plot (Figure 4.7) illustrates boundaries where choices of Φ_1 and Φ_2 lead to a specific bursting rhythm, which can be thought of as a stable fixed point in (Φ_1, Φ_2).

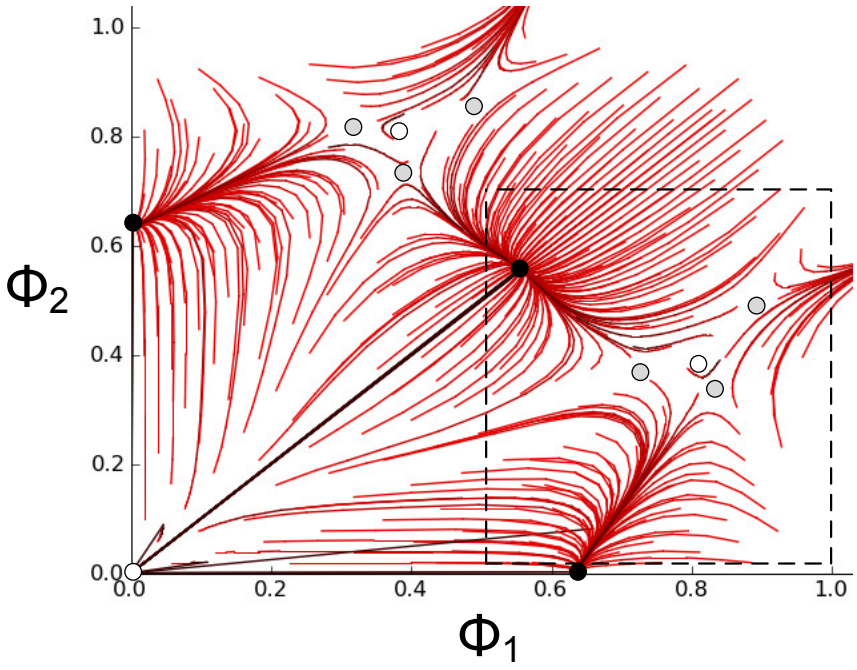

Figure 4.7. Phase portrait for the weakly coupled symmetric motif ($g_{ij} = 0.005$; settle cycles = 25). Saddle nodes are indicated in grey, unstable foci and nodes are indicated in black, and stable nodes are indicated in black.

As shown, there are clearly trajectories that both converge towards the center (0.468,0.468) and repel from the origin. Additionally, there appear to be two other stable equilibria, corresponding to the fixed points (0,0.468) and (0.468,0). A magnification of one of the regions shows trajectories moving away from an unstable focus (Figure 4.8). Moreover, the trajectories move away along asymptotes, indicating the presence of three saddle equilibria surrounding the unstable focus. Figure 4.9 illustrates an

example of this type of non-linear trace whose initial phase shift conditions exist near the unstable focus. Additional test simulations around those regions also provide data suggesting this. Finally, superimposition of the phase shift plots as well as the parameterized phase plots illustrate that unstable and saddle activity occurs around the triangular shaped gray regions corresponding to out of phase (or possibly aperiodic) burst rhythms (Figure 4.10).

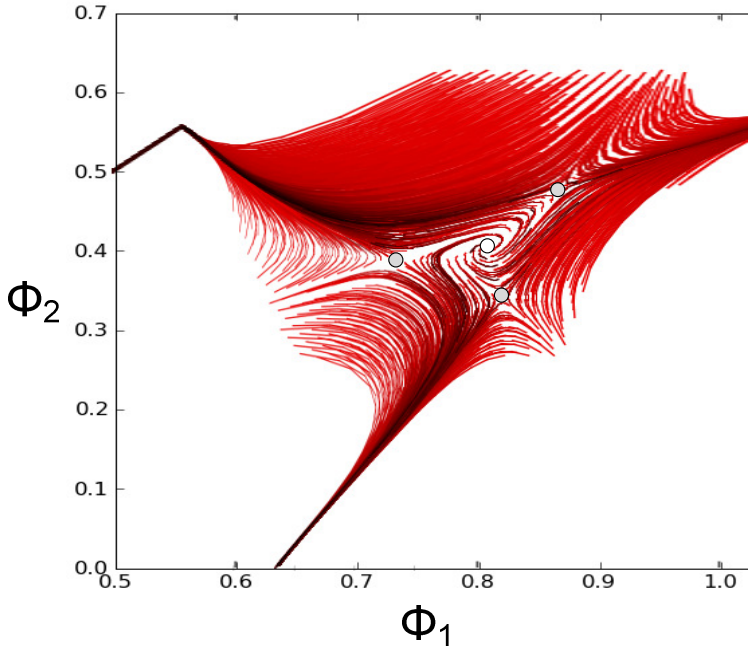

Figure 4.8. Magnification of phase portrait region around the unstable focus (g_{ij} = 0.005; settle cycles = 25). Inset corresponds to the dashed region in Figure 4.6. Saddle nodes are indicated in gray, unstable foci are indicated in black.

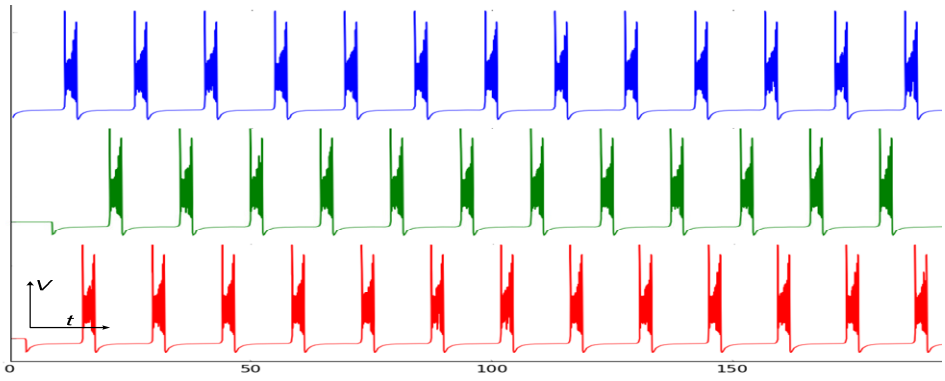

Figure 4.9. Voltage trace with phase shift near the unstable focus; (Φ_1, Φ_2) = (0.78,031).

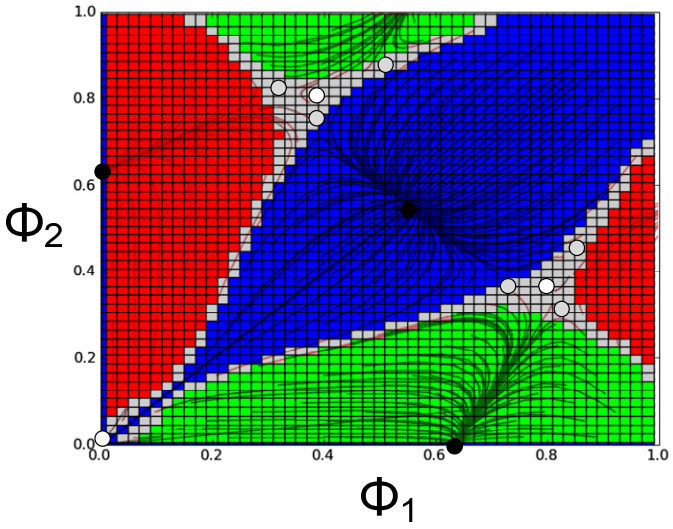

(a)

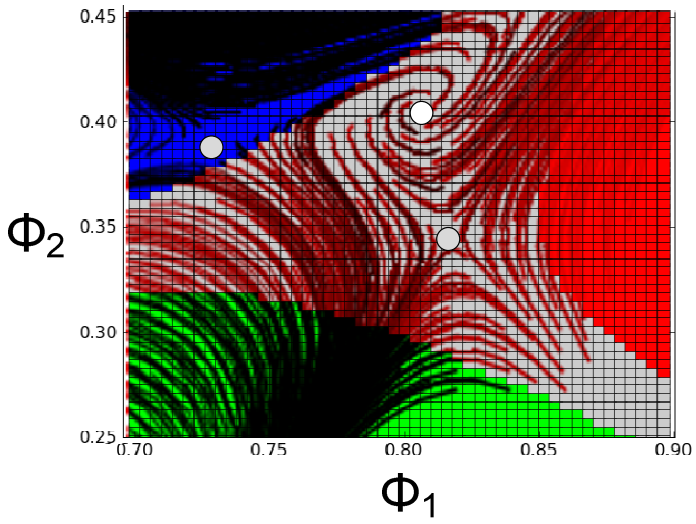

(b)

Figure 4.10. Superimposition of the phase shift diagram and the phase portrait for symmetric weakly coupled case. (a) Complete planar view. (b) Magnified view near one of the unstable foci.

In order to more clearly illustrate the relative locations of each of the equilibria present in the symmetric weakly coupled motif (Figure 4.11), we show a simplified phase trace diagram indicating the directions taken by trajectories originating in the basins of attraction.

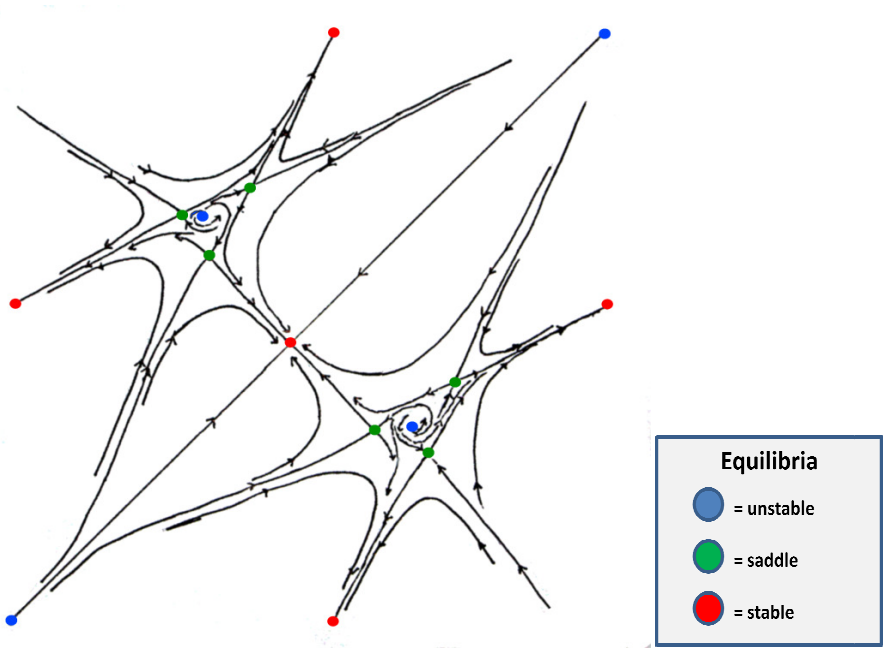

Figure 4.11. Simplified rendering of the phase portrait for the weakly coupled symmetric case.

Next, we consider that the phase shifts are of unit modulus and that the regions shown above are symmetric with respect to the line $\Phi_1 = \Phi_2$. Because of this symmetry, the phase shift plot can be thought of as being on a torus (shown in Figure 4.12), where convergence to bursting rhythms (i.e. stable fixed points) occurs along the surface. As before, the traces in red indicate phase shift trajectories that converge towards stable equilibria as well indicate regions were saddle nodes and unstable foci are present, whereas the white region shown is a repelling basin along the torus.

The single winner and winnerless outcomes described previously correspond to a specific case for V_{K2}^{shift} with g^+ fixed in both directions. Recall that for the leech heart interneuron model V_{K2}^{shift} is used as the bifurcation parameter in order to produce the dynamics associated with bursting activity, and that the outcome of an individual neuron's burst is subject to a shift of bifurcations mapped in Figure 3.1. We adjust this parameter from a relatively stable value of V_{K2}^{shift} = -0.01875 to V_{K2}^{shift} = -0.02150 and plot phase portraits ($\Delta\Phi$= 0.05) for each case (Figure 4.13).

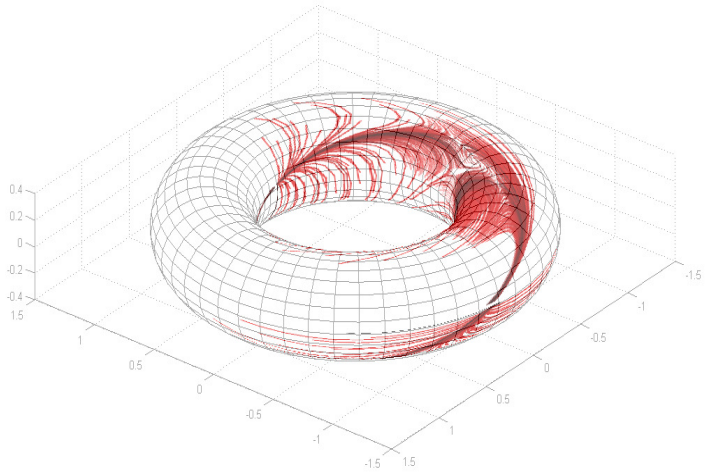

Figure 4.12. The phase portrait for the weakly coupled symmetric case represented on a torus.

While the scope of this study is inadequate to fully explain the mechanics that transpire as V_{K2}^{shift} is lowered, it is clear that the transitions are dramatic and strongly influence the bursting patterns exhibited in the motif. We note that for V_{K2}^{shift} =-0.01875 there exists two invariant circles that appear to dissipate before V_{K2}^{shift}=-0.019, leaving only the unstable foci and the stable equilibria. As V_{K2}^{shift} decreases, the scenario gets more complicated; new, distinct equilibria points appear along the axes, suggesting that two of the single winner scenarios (red and green) may have more than one numerical outcome for some values of V_{K2}^{shift}. We also note that some separatrices become more strongly stable (shown Figure 4.13 via the transition from red to black as each trajectory is calculated), meaning that trajectories tend to converge rapidly to a separatrix well before it approaches the neighborhood of the corresponding stable equilibrium. These distinct outcomes continue to persist, even as other dynamics change in the Φ_1- Φ_2 plane. We finally note that the appearance of a stable focus around V_{K2}^{shift}=-0.0215 as well as the sudden disappearance of saddle nodes that previously persisted in the region.

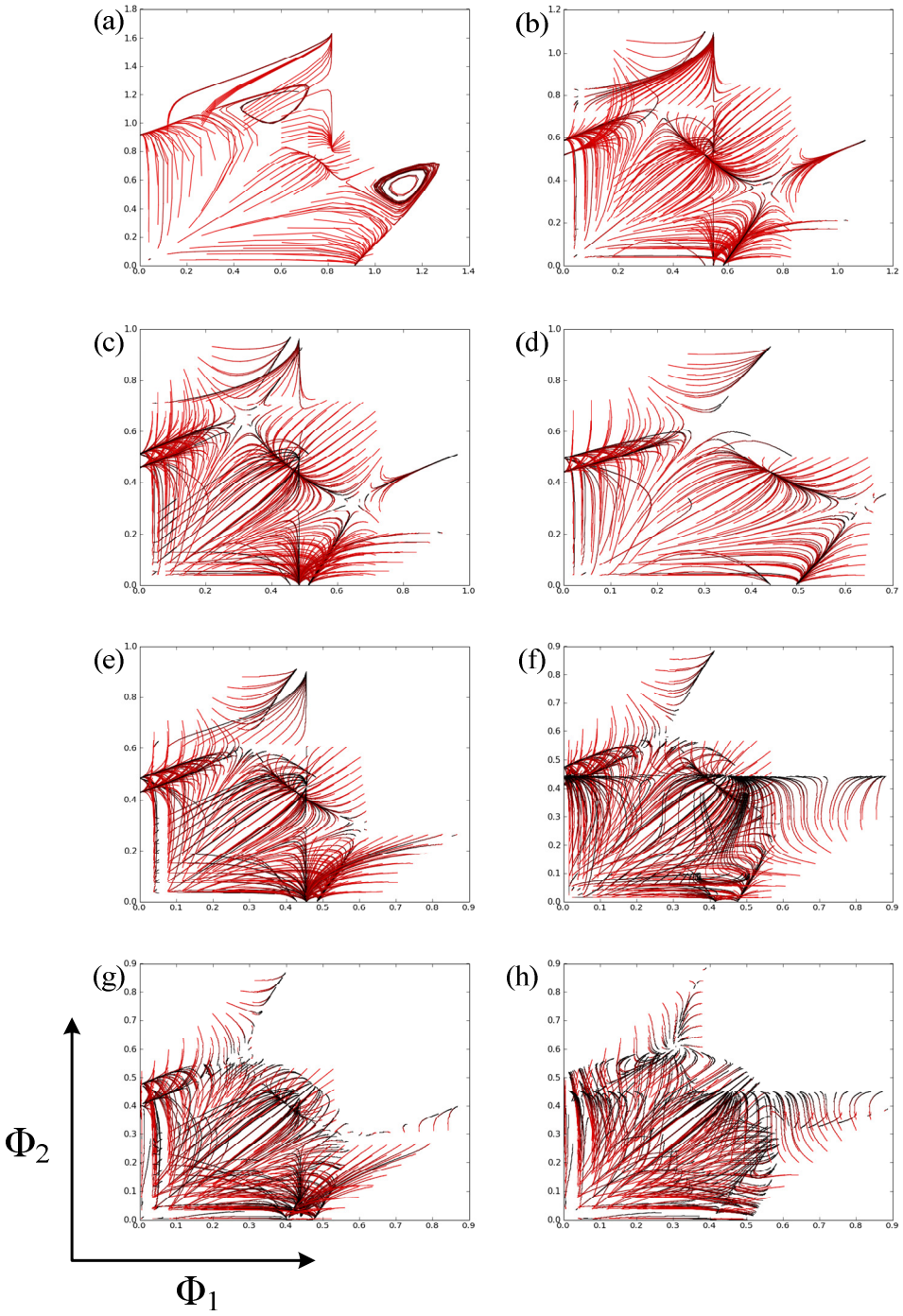

Figure 4.13. Phase portraits for the symmetric weakly coupled motif with g=0.0005, and varying V_{K2}^{shift}. Note the appearance of two invariant circles (inset a) that disappear, as unstable foci and saddle nodes produce dynamics that give rise to multiple equilibria states (insets b-g). As V_{K2}^{shift} is lowered further, more dynamics begin to emerge, include a stable focus (inset h). (a) V_{K2}^{shift} = -0.01875; (b) V_{K2}^{shift} = -0.01912; (c) V_{K2}^{shift} = -0.01950; (d) V_{K2}^{shift} = -0.01975; (e) V_{K2}^{shift} = -0.02000; (f) V_{K2}^{shift} = -0.02050; (g) V_{K2}^{shift} = -0.02100; (h) V_{K2}^{shift} = -0.02150.

Weakly Coupled Motifs: Asymmetric Cases

For the weakly coupled asymmetric we fix V_{K2}^{shift} = -0.019 and adjust the clockwise synaptic coupling strengths g^+, but only proportionate to g^- so that the motif remains essentially weakly coupled. Phase portraits are plotted similar to the traces generated in Figure 4.7 for the symmetric motif. The results of this asymmetric adjustment are shown in Figure 4.14 as g^+ is varied between 0.0009 and 0.0020.

Prior to g^+=0.0008 there appears to be no unusual behavior. Beginning at this point, the top unstable focus begins to weaken with respect to the unstable focus on the lower right. Recall that for the symmetric case both unstable foci are surrounded by three saddle nodes. As g^+ increases the lower focus begins to become a stable attractor as saddle separatrices begin to tend towards it (Figure 4.14b). Increasing g^+ further we begin to see the saddle nodes themselves begin to merge with the newly stable focus and eventually vanish (Figure 4.14d). The upper unstable focus because more strongly repelling, with trajectories in the region rapidly tending towards an equilibrium or the newly formed stable focus. From the perspective of bursting rhythms, the convergence of many trajectories to the stable focus around (0.666, 0.333) suggests a large basin of attraction for the 1-3-2 winnerless state, an outcome not observed at all in the strongly coupled case, where all desynchronized burst outcomes were of the order 1-2-3.

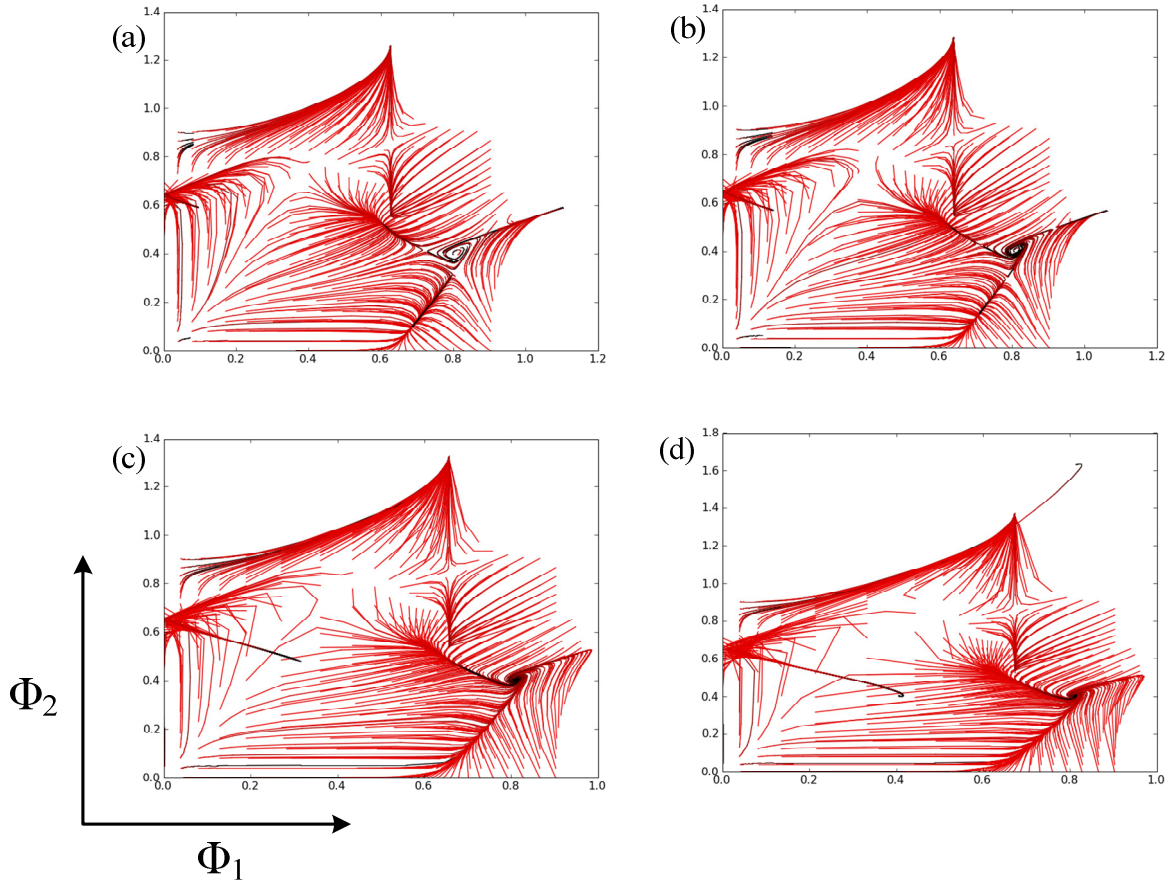

Figure 4.14. Phase portrait diagrams for the weakly coupled asymmetric cases. The increased asymmetry begins causes the unstable focus to become stable (insets a-b), and eventually cause its neighboring saddle nodes to converge and vanish (insets c-d). The location of the stable focus indicates a 1-3-2 bursting outcome in the motif. (a) g^{+}=0.0009; (a) g^{+}=0.0011; (a) g^{+}=0.0015; (a) g^{+}=0.002;

5. DISCUSSION

Summary

The oscillatory attractors of the network correspond to specific burst rhythms, which are thought to be associated with a particular type of locomotive activity of a CPG. Each burst rhythm that can be produced by the motif functions as an oscillatory attractor of the system with respect to the phase shifts of each cell. By varying the strength of the asymmetric coupling in the strongly coupled motif, we observe bursting regimes that ultimately cascade into desynchronized burst rhythms. Because of the large coupling strengths involved, synchronization to any of the possible bursting patterns is quite rapid, even in the case of the "chaotic" regime when $g^{+}\approx 0.70$, where the phase shifts are measured for different fixed numbers of settle cycles. The appearance of the winnerless state region does not result from a specifically bounded region appearing and growing as g+ is increased. Instead the region results from a gradual tendency of single winner outcomes in the upper diagonal region of the Φ_1- Φ_2 plane to slowly give way to winnerless states, regardless of the orginal bursting rhythm. Once the cascading regions of burst states appear more rapidly, a large desynchronized burst region appears almost instantly afterwards. We also note that the burst order in the winnerless state is constant (1-2-3) regardless of our subsequent choice of g^{+} or initial phase conditions in $\Phi_1 x \Phi_2$.

To observe the attractors and repellers of the phase system, we utilize a weak coupling motif that produces a slower rate of synchronization between the burst patterns within the network. Very specific dynamics arise when the phase portrait for the symmetrically coupled case $g_{ij} = 0.0005$ is computed. There exist three stable fixed points corresponding to the known burst rhythm outcomes where one cell is in anti-phase with respect to the others. More notably, there exists a repeller at the origin, which suggests that unless the phase shift is identically (0,0), the burst pattern will always tend to one of the other regions, which correspond to either single winner dynamics or a winnerless state. Also of notice is the appearance of unstable focus surrounded by three saddle nodes. When we examine the asymmetric weak

cases, we observe transitioning dynamics where one of the unstable foci becomes stable, and all three of its neighboring saddles collapse onto it. We also find that with the newly formed stable focus, the burst order outcomes for winnerless states appear to be different than those observed in the strongly coupled asymmetric case. When we increase the length of the burst by lowering V_{K2}^{shift}, we see the emergence of different dynamics altogether, where multiple equilibria arise for each of the single winner states, and separatrices begin to shift considerably. The comprehensive dynamics occurring here are not yet fully understood, but it does suggest that adjusting the length of the burst has a significant effect on the type of bursting patterns that can arise in the motif, just as the length of the burst for a single neuron influences its capacity to exhibit tonic spiking and bursting states.

Further Directions

This effort yields some insight into the basins of attraction that are produced when different phase shifts are introduced to an inhibitory motif, but certainly behaviors observed in the study remain open to qualification. For the strongly coupled cases, we intend to investigate the dynamics that give rise to the cascading burst rhythms. Additionally, anti-phase (but not necessarily aperiodic) states should yield a series of attractors as well, although these have not been characterized in the work shown. However, transitioning attractors of oscillating networks from different stability states have been observed in similar Hodgkin-Huxley based models (Rabinovich, 2007).

The basins of attraction for the weakly coupled case are significantly different from the strongly coupled case, and as a result the range of bursting outcomes appears to be very different as well. One possible way to observe this change in dynamics would be to identify the coupling strengths g_{ij} where the system tends from a weakly coupled motif to a strongly coupled one. Additionally the dynamics that arise when the burst length of each cell is adjusted via V_{K2}^{shift} become seemingly complex and require further investigation to determine the underlying bifurcations that give rise to these transitions.

Numerical computation of the separatrices and eigenvalues associated with these shifting equilibria would aid in efforts aimed in this direction.

The measurements made with regard to phase shift are isochronic, i.e. Φ_1 and Φ_2 are discretized with respect to the isolated period. Because of this, more phase shift values are evaluated during the "slow" portion of burst cycle (quiescence) than the "fast" portion (tonic spiking). To rectify this, it has been proposed that the isolated periodic orbit be spliced into equal intervals in phase space as opposed to time, from which the phase shift time values would be interpolated.

Finally many of the constructions used thus far in our investigation into the multistable outcomes for the inhibitory motif can be extended mixed CPG motifs (where inhibitory and excitatory signals are passed) as well as motifs with a larger population would potentially yield understanding of the complex dynamics generated by those networks. Our study here provides the construction of a methodology for observing the emergence of dynamics in both symmetric and asymmetric networks as well as seeks to establish a relationship between the burst outcomes and behaviors present in strongly coupled motifs, where outcomes are decided very rapidly, and the slower, more traceable dynamics that are found in weakly coupled systems.

REFERENCES

Ashwin, P., Burylko, O., and Maistrenko, Y. (2008). Bifurcation to heteroclinic cycles and sensitivity in three and four coupled phase oscillators. *Physica D.* **237**:454-466.

Canavier, C. C., Baxter, D. A. , Clark, J. W., and Byrne, J. H. (1999). Control of multistability in ring circuits of oscillators. *Biol. Cybern.* **80**:87-102.

Cazelles, B., Courbage, M., and Rabinovich, M., (2001). Anti-phase regularization of coupled chaotic maps modeling bursting neurons. *Europhys. Lett.* **56**(4):504-509.

Channell, P., Cymbalyuk, G., Shilnikov, A. (2007). Origin of bursting through homoclinic spike adding in a neuron model. *Phys. Rev. Lett.* **98:**134101.

Clewley, R. H., Sherwood, W.E., LaMar, M.D., Guckenheimer, J.G. PyDSTool dynamical systems software, 2004. http://pydstool.sourceforge.net

Clewley, R., Soto-Trevino, C., Nadim, F. (2009). Dominant ionic mechanisms explored in the transition between spiking and bursting using local low-dimensional reductions of a biophysically realistic model neuron. *J. Comp. Neurosci.* **26**(1):75-90.

Cymbalyuk, G., Gaudry, Q., Masino, M., Calabrese, R. (2002). Bursting in Leech Heart Interneurons: Cell-Autonomous and Network-Based Mechanisms. *J. Neurosci.* **22**(24):10580-10592.

Cymbalyuk, G., Shilnikov, A. (2005). Coexistence of tonic spiking oscillations in a leech neuron model. *J. Comp. Neurosci.* **18**:255-263.

Cymbalyuk, G., Calabrese, R. and Shilnikov, A. (2005). How a neuron model can demonstrate co-existence of tonic spiking and bursting? *Phys. Rev. E* **81**(5):056214.

Gutkin, B., Pinto, D. and Ermentrout, B. (2003). Mathematical neuroscience: from neurons to circuits to systems. *J. Physiology* **97**:209-219.

Izhikevich, E. M. (1999). Neural excitability, spiking, and bursting. *Int. Jour. of Bifurcation and Chaos* **10**(6):1171-1266.

Izhikevich, E. M. (2002). Synchronization of Elliptic Bursters. *SIAM Rev.* **43**:315-344

Izhikevich, E., 2007. *Dynamical Systems in Neuroscience: The Geometry of Excitability and Bursting.* Cambridge: MIT Press. 441 p.

Jalil, S., Belykh, I., Shilnikov, A. (2009). Synchronized bursting: the evil twin of the half-center oscillator. *PNAS*, paper pending.

Marder, E., and Calabrese, R. (1996). Principles of Rhythmic Motor Pattern Generation. *Physio. Rev.* **76**(3):687-717.

Nowotny, T., and Rabinovich, M. (2007). Dynamical origin of independent spiking and bursting activity in neural microcircuits. *Phys. Rev. Lett.* **98**:128106.

Rabinovich, M. I., Varona, P., Selverston, A. I., Abarbanel, H. D. I. (2006). Dynamical principles in neuroscience. *Rev. Mod. Phys.* **78**(4):1213-1265.

Rinzel, J. (1987). A formal classification of bursting mechanisms in excitable systems. In: A. Gleason, ed. Proceedings of the International Congress of Mathematicians, American Mathematical Society, Providence, RI, 1578-1594.

Rulkov, N. F. (2002). Modeling of spiking-bursting neural behavior using two-dimensional map. *Phys. Rev. E*, **65:**041922.

Rulkov, N. F., Timofeev, I., and Bazhenov, M. (2004). Oscillations in large-scale cortical networks: map based model. *J. Comp. Neurosci.* **17**:203-223.

Shilnikov, A. L., Rulkov, N. F. (2002). Origin of chaos in a two-dimensional map modeling spiking-bursting neural activity. *Int. Jour. of Bifurcation and Chaos* **13**(11): 3325-3340.

Shilnikov, A., Rulkov, N. F. (2004). Subthreshold oscillations in a map-based neuron model. *Phys. Lett. A.* **328**:177-184.

Shilnikov, A., Cymbalyuk, G. (2004). Homoclinic bifurcations of periodic orbits en a route from tonic-spiking to bursting in neuron models. *Regular and Chaotic Dynamics* **9**(3):281-297.

Shilnikov, A., and Cymbalyuk, G. (2005). Transition between tonic spiking and bursting in a neuron model via the blue-sky catastrophe. *Phys. Rev. Lett.* **94**:048101.

Shilnikov, A. L., Gordon, R., Belykh, I. (2008). Polyrhythmic synchronization in bursting networking motifs. *Chaos* **18**:1-13

Shilnikov, A., Kolomiets-Shilnikova, M. (2008). Methods of the Qualitative Theory for the Hindmarsh-Rose Model: A Case Study. A Tutorial. *Int. Jour. of Bifurcation and Chaos* **18**(8):2141-2168.

Sporns, O., Kotter, R. (2004). Motifs in brain networks. *PLoS Biology* **2**(11):1910-1918.

Terman, D. *An Introduction to Dynamical Systems and Neuronal Dynamics.* 2004. (PDF)

Terman, D. Rubin, J. E., Yew, A. C., and Wilson, C. J. (2002). Activity Patterns in a Model for the Subthalamopallidal Network of the Basal Ganglia. *J. Neurosci.*, **22**(7):2963-2976.